Composite Structures 319 (2023) 117113

Contents lists available at ScienceDirect

Composite Structures

journal homepage: www.elsevier.com/locate/compstruct

# Debonding sawtooth analytical model and FE implementation with in-house experimental validation for SRG-strengthened joints subjected to direct shear

Natalia Pingaro, Angelo Savio Calabrese, Gabriele Milani *, Carlo Poggi

*Politecnico di Milano, Department of Architecture, Built Environment and Construction Engineering, Milan, Italy*

ARTICLE INFO

*Keywords:*
Debonding mechanisms
SRG reinforcement
Sawtooth multi-linear approximation
Bond-slip model
FE models with cutoff bars

ABSTRACT

A novel and simple analytical debonding model for Steel Reinforce Grout (SRG)-strengthened specimens subjected to direct shear tests is proposed. All the nonlinearity is lumped at the interface between reinforcement chords and mortar, the substrate is assumed perfectly glued to mortar, infinitely stiff and resistant and the steel grid is considered linear elastic. The non-linear interface tangential stress-slip relationship is assumed discontinuous and multi-linear and constituted by four phases, three elastic with progressively reduced stiffness and the last perfectly plastic. The assumption of a non-vanishing residual tangential strength is paramount to reproduce the typical pseudo-linear hardening observed experimentally in the global force-displacement curves when the debonding frontier is triggered starting from the loaded edge. Under such hypotheses, the second order differential field equation describing the slippage of the reinforcement on the support admits closed form solutions, which are suitably derived. An implementation into a standard Finite Element (FE) commercial code is also proposed, which relies in a discretization of the reinforcement through three cutoff bars (one ductile and two brittle) disposed in-parallel, elastic elements for the steel grid and rigid beams used as transversal connections. The reliability of the sawtooth and the FE models is assessed by means of a thorough comparison with experimental data obtained by the authors for this purpose testing five replicates of a concrete specimen strengthen with a SRG and subjected to a standard shear test.

## 1. Introduction

Existing reinforced concrete and masonry structures need very frequently rehabilitation or upgrading for a variety of reasons, which include -but are not limited to- a change of the intended use, an increase of the loads or the need to improve the load carrying capacity for seismic actions. In this context, fiber reinforced composites represent an interesting solution for strengthening and retrofitting existing structural elements, because they can be applied externally, and hence very rapidly, with very low invasiveness and without requiring the partial or total inhibition of use. Among them, Fiber Reinforced Polymer (FRP) composites were the first used and they gained tremendous popularity in the 90 s, thanks to their excellent mechanical and chemical properties, such as for instance the high strength-to-weight ratio, and the relatively limited curing time. Pretty soon, however, it was understood that FRP strips glued to a brittle support exhibit also many drawbacks, such as an abrupt drop of the performance at relatively high temperatures, excessive stiffness, problems of vapor permeability and the irreversibility of the intervention, which is considered unacceptable in historical and heritage structures.

To overcome such major limitations, organic binders used in combination with fiber sheets and strips were substituted with inorganic ones with embedded fiber grids, and a new generation of high strength composite materials has been recently proposed [1], named Textile Reinforced Mortar (TRM), or also Fiber Reinforced Cementitious Matrix (FRCM). The acronym SRG is also quite common, which stands for Steel Reinforced Grout. It is a special TRM constituted by a reinforcement made by steel cords formed by interwoven steel wires embedded in a cementitious grout matrix.

To investigate the bond behavior of the inorganic-matrix composite, small Reinforced Concrete (RC) specimens, strengthened with SRG and subjected to standard single lap shear tests can be considered. The role of experiments is fundamental to perform numerical analyses of structural elements reinforced with SRG. In particular, the knowledge of elastic

* Corresponding author.
*E-mail address:* gabriele.milani@polimi.it (G. Milani).

https://doi.org/10.1016/j.compstruct.2023.117113
Received 16 December 2022; Received in revised form 19 March 2023; Accepted 3 May 2023
Available online 8 May 2023

stiffness, ultimate load-carrying capacity and ductility of the specimen assume a crucial relevance for the calibration of the models.

The observed modes of failure are various, depending on the mechanical properties of the different materials constituting the reinforcement (for a comprehensive review the reader is referred for instance to [2-5]), but previous studies have proven that to lump non linearity at the reinforcement-support interface is an effective and sufficiently straightforward strategy which can be used in practice.

There is another advantage coming from experimental information that may be useful to tune the mechanical properties of the interface, namely the fact that the interface stress-slip law can be deduced also having at disposal only the experimental measure of the slip at the loaded edge [67]. This is an important feature for TRM reinforcement, where it is not an easy task to monitor the strains along the bonded length, because of the presence of the external mortar layer. To embed strain gauges along the bonded length or to use DIC seems much less useful than the counterpart proposed for FRP [8] because of the presence of the external mortar layer, whereas the utilization of optic fibers [9] may be an alternative, which however turns out to be costly, requires trained technicians and may perturbate the specimens for the presence of the sensor wires.

As far as the numerical/analytical procedures available are concerned, there are in the literature some models at disposal. In [10-16] and [17], multi-linear or exponential-softening laws for the interface were assumed, both having the advantage to provide closed form solutions in case of flat specimens. In some other publications [18-22], the field problem (which mathematically translates into a second order differential equation) is solved as a standard Boundary Value Problem BVP, or less frequently transformed into a Cauchy's Problem, which has the advantage of being fully explicit. However, the direct implementation into a commercial FE code to perform analyses on real structures needs the implementation of ad-hoc subroutines. Furthermore, a closed form solution can be derived exclusively for interfaces whose stress-slip relationship is either multi-linear or exponential, being in any case affected by a specificity of the model proposed that is difficult to adapt in the most general case, e.g. for curved substrates. In [23], a more sophisticated approach is proposed, where the elastic reinforcing grid and the internal brittle mortar are modeled separately and interact with a non-linear interface. A non-linear system of differential equations is obtained, transforming a standard boundary value problem into a Cauchy's one, then solved with a classic shooting technique. The idea to disregard one of the mortar layers is in common with [5], where however the mortar layer is assumed elastic-perfectly fragile. Whilst the procedure appears rather appealing because able to give locally much more information on the debonding phenomenon in TRM reinforced specimens, it is still a rough approximation because the external layer of mortar is disregarded and again the direct implementation into a FE software appears nonobvious. A straightforward alternative is to adopt a FE discretization just from the beginning, see e.g. [24-32], and to use the galleries of elements and material models that are put at disposal by the specific software utilized, clearly constraining the user to carry out computations with a software that is not specifically crafted for a specific, highly complex, mechanical problem. Anyway, what is clear from a thorough review of the existing literature is that there is still a large gap to fill between interpretation of the experimental data on small samples and applicability in demanding numerical analyses carried out to reproduce the behavior of realistic examples of reinforced structural elements, which is the main aim in common design and the final target of the present research. An interesting breakthrough in this regard has been recently obtained in [33] for FRP, where the interface between reinforcement and substrate has been modeled by means of a sawtooth bilinear constitutive relationship, which has been then implemented directly into a low-cost commercial FE software using two elasto-fragile trusses disposed in-parallel with identified mechanical properties and linked together by rigid beams. The advantage is evident, giving the possibility to analyze even complex case studies through a FE commercial software equipped only with truss elements whose non-linear behavior is as simple as possible, namely elastic-perfectly fragile. At the same time, the flexibility appears rather high, allowing the study of a variety of cases truly interesting in engineering practice. The aforementioned procedure is however specifically conceived for FRP and is unable to adapt properly to TRM, where the possible presence of a residual tangential strength at the interface for sufficiently large slip values may be responsible for a global debonding characterized in the global force-slip curve by a pseudo-linear hardening. To cope with such feature -which is commonly observed in experimentation- there is the need to model the interface by means of at least three in-parallel trusses, two of them elasto-fragile and the other elastic-perfectly plastic. On the other hand, concerning the adoption of a sawtooth model to characterize the constitutive behavior of materials exhibiting softening -in this case the interface-, its reliability is already notorious from the literature [34-38], as well as the related advantages, which are essentially a consequence of the fact that the non-linear behavior is simply derived as a sequence of elastic stages, for which in some cases -as the present one- closed form solutions can be retrieved.

The present paper discusses an evolution of such multi-linear elasto-fragile truss approach, and its suitability when applied to TRM reinforcing systems is proved thorough a comprehensive comparison with experimental data obtained by means of a campaign conducted in house. It relies in five RC samples reinforced with SRG and tested in single lap shear. The advantage to carry out a new experimentation is that there is the possibility to characterize experimentally all those mechanical parameters of the model that are needed, without assuming some data arbitrarily. The model adopted at the interface is a sawtooth interface stress-slip relationship characterized by four phases, the first three linear elastic with progressively degraded stiffness and the last assumed perfectly plastic. Such sawtooth model is then implemented directly in a commercial FE software, using three in-parallel cutoff bars, the first two elasto-brittle, the third elastic-perfectly ductile. One interesting feature is that the differential equation field obtained in the different phases active is of second order, homogeneous with constant coefficients for three of the four phases, and with separable variables when the residual interface strength is activated. In both cases, a closed form solution is found easily, whose constants of integration are retrieved by imposing suitable boundary conditions. The only complication stands in establishing the points of triggering of the different phases; in the paper, an analytical approach is proposed, which allows a direct estimation of such points. A procedure of identification based on fracture energy is then setup, to secure that the sawtooth, discontinuous and piecewise linear constitutive relationship adopted at the interface is equivalent to the actual continuous one obtainable with suitable experimental data reduction.

The paper is organized as follows: in Section 2, the original sawtooth model with its FE implementation is illustrated and a procedure to obtain the global force–displacement curve of standard shear tests is discussed. Dealing with the commercial FE software, the implementation proposed uses exclusively cutoff bars disposed in-parallel and rigid beams connecting them. In Section 3, the in-house single-lap direct shear experimental tests carried out to validate the analytical/numerical model are discussed and the experimental interface constitutive law is deduced, identifying a continuous trilinear relationship to compare with. In Section 4, the numerical results obtained with the sawtooth model are then comprehensively discussed and compared with experimental evidences. Section 5 is then devoted to the numerical implementation of the approach proposed in a commercial FE software equipped only with elasto-perfectly fragile and elasto-perfectly ductile trusses. Finally, Section 6 draws some conclusions and discusses the future developments, with particular attention to the application of the model for the analysis of entire structures reinforced with TRM.

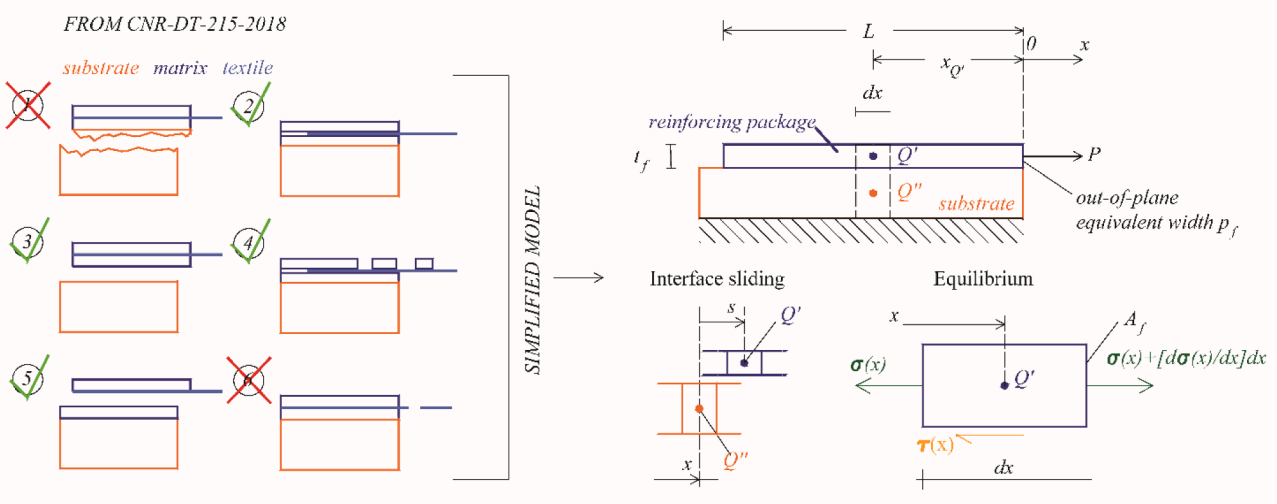


**Fig. 1.** Flat rigid support strengthened with SRG, equilibrium of the reinforcing pack.

## 2. The analytical (sawtooth) and FE numerical (with cutoff bars CoBs) approach proposed

The aim of the section is to present a novel analytical sawtooth model with direct FE numerical implementation in a commercial software for the prediction of the debonding behavior of SRG strengthened specimens subjected to standard shear tests. The term "direct" means here that there is no need to implement new subroutines into a FE code, but that the implementation is simply possible meshing the strengthening package by means of a network of in parallel Cutoff Bars (CoBs) -which are truss elements with limited tensile strength and post elastic behavior assumed either elasto-perfectly fragile or elasto-perfectly-ductile- connected one each other by rigid beams and externally linked to the substrate (assumed rigid) and the steel strands, modeled with elastic trusses.

Section 2.1 illustrates first the mono-dimensional theoretical model adopted to investigate the SRG debonding from a substrate. Following a classic literature in the field, the strengthening package is modeled with an elastic layer representing the SRG strands and an inelastic interface between steel and substrate. Then, the sawtooth model is introduced to characterize the interface constitutive behavior and a closed form solution is derived to deduce slip and stress distribution along the bond length.

The second subsection finally discusses the direct implementation of the sawtooth model into a commercial FE software through CoBs and rigid connection beams.

### 2.1. Analytical sawtooth model

Let us consider a SRG strengthening package, as reported schematically in Fig. 1, bonded to a sufficiently stiff and resistant substrate. According to a quite consolidated approach already adopted by many authors in the literature, the different layers of the reinforcement are not modeled separately and the non-linearity is lumped exclusively at the interface between an elastic layer of steel strands and the rigid substrate. Implicitly, lumping non linearity exclusively there, it is assumed that failure occurs for a progressive inelastic slippage of the steel strands with respect to the matrix where they are embedded. More precisely, it can be stated that, since the constitutive behavior of the conventional interface can be deduced from experimental data, as it will discussed in the following Section 3.4, such approach renounces to predict which kind of failure mode is triggered in reality, providing information exclusively on the expected global behavior.

All the aforementioned issues considered, making the assumption that failure occurs at the interface between matrix and fabric and that damage is not localized in the substrate - which is considered rigid and infinitely resistant-, the mechanical system studied is a layer of elastic steel bonded to the substrate by means of a fictitious non linear interface where all inelastic phenomena take place. The elastic layer is assumed subjected to a monoaxial state of stress, acting along the longitudinal direction. Its cross area is $A_f = nA_{fs}$ and the interface equivalent width is $p_f = np_{fs}$, where $A_{fs}$ and $p_{fs}$ are respectively area and perimeter of the single strand. The only independent kinematic variable is the longitudinal displacement of the elastic layer along the bond length. The hypothesis of rigid support makes, at the abscissa $x$, the sliding $s(x)$ between steel strands and support equal to the longitudinal displacement of the elastic layer. Because of the non-null slip $s(x)$, a tangential stress $\tau(x)$ is transferred from the steel elastic layer to the support through the interface. In such model, the interface is therefore assumed subjected to a pure Mode-II fracture.

Imposing the equilibrium along the longitudinal direction of an infinitesimal portion $dx$ of the strands (see Fig. 1) the following equation can be written:

$$\tau = \frac{A_f}{p_f}\frac{d\sigma}{dx} \tag{1}$$

Where $\sigma$ is the axial stress of the strands and $\tau$ is the shear stress at the interface, which is a function of the sliding $s$. On the other hand, the constitutive elastic relationship of the strands allows to write the following equation:

$$\frac{d\sigma}{dx} = E_f\frac{d^2s}{dx^2} \tag{2}$$

where $E_f$ is the Young modulus of the strands and all the other quantities have been already introduced. Substituting (1) into (2) it is possible to deduce the following second order field differential equation:

$$\frac{d^2s}{dx^2} - \frac{p_f\tau}{E_fA_f} = 0 \tag{3}$$

It is worth mentioning that Eq. (3) is nonlinear if the $\tau - s$ law is inelastic.

Zou et al. showed in [39] that, assuming a trilinear $\tau - s$ law for the interface characterized by an initial elastic phase followed by a linear softening which precedes a horizontal plateau having residual strength, it is possible to derive a closed form solution for the debonding problem. However, such interface trilinear law is generally not available in standard commercial FE codes and ad-hoc subroutines should be implemented to give the possibility to study real scale reinforced structures. It is therefore nothing more than a good reference to compare

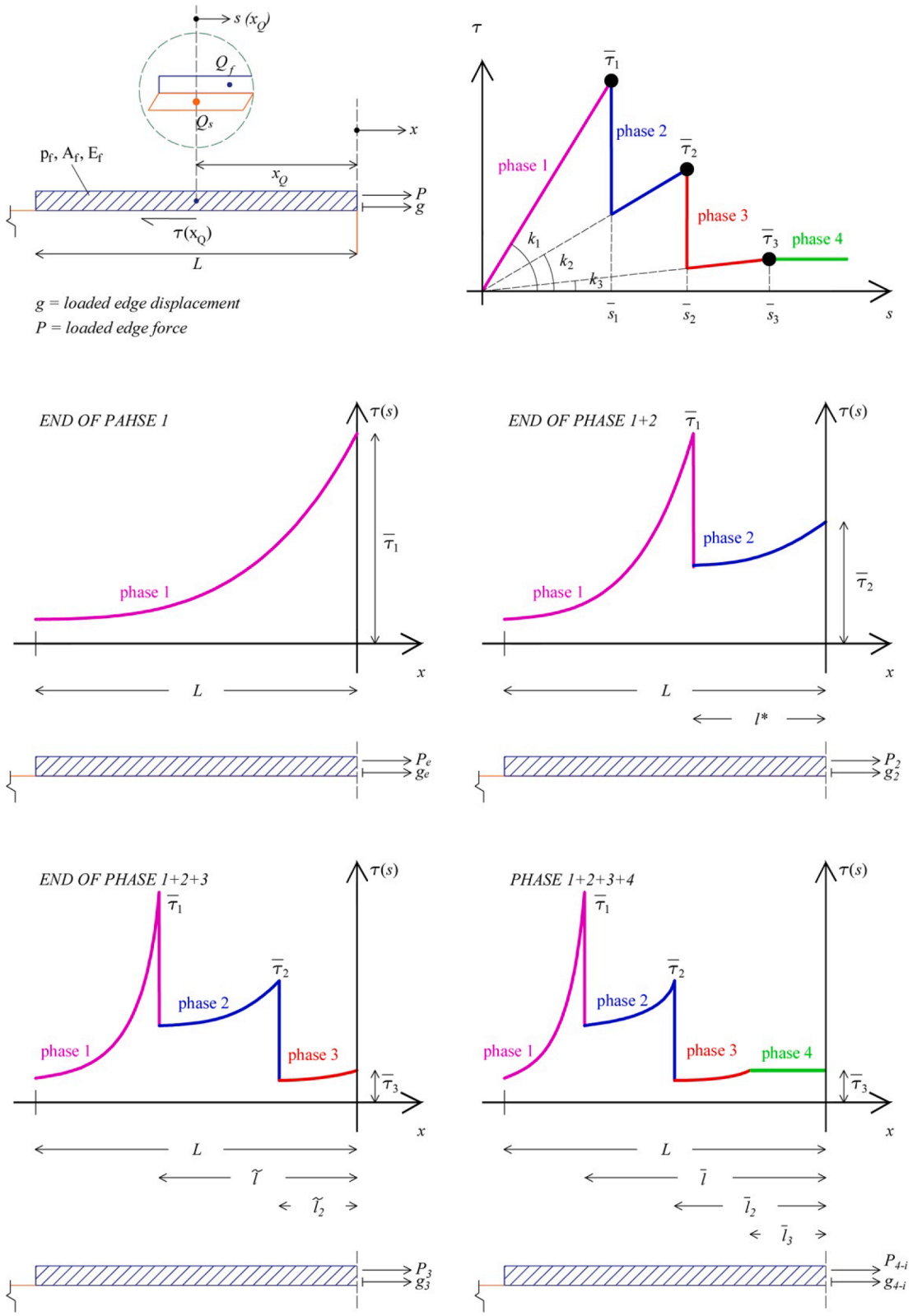


**Fig. 2.** End of phases of the sawtooth analytical interface model.

with to benchmark a more straightforward approach applicable in common engineering practice.

With such need in mind, the main idea here proposed is to consider a sawtooth $\tau - s$ interface relationship, see Fig. 2. More in detail, the model is characterized by three phases with progressively reduced stiffness plus a final horizontal plateau (4 phases in total). The first phase corresponds to the elastic stage of the trilinear $\tau - s$ law, phases 2 and 3 approximate the descending branch and the last phase corresponds to the trilinear plateau. The advantage is that field equation (3) admits always an analytical solution -because all phases are elastic (except the last one)- and the global behavior can be obtained simply identifying the regions where the different phases are active, without the need to utilize

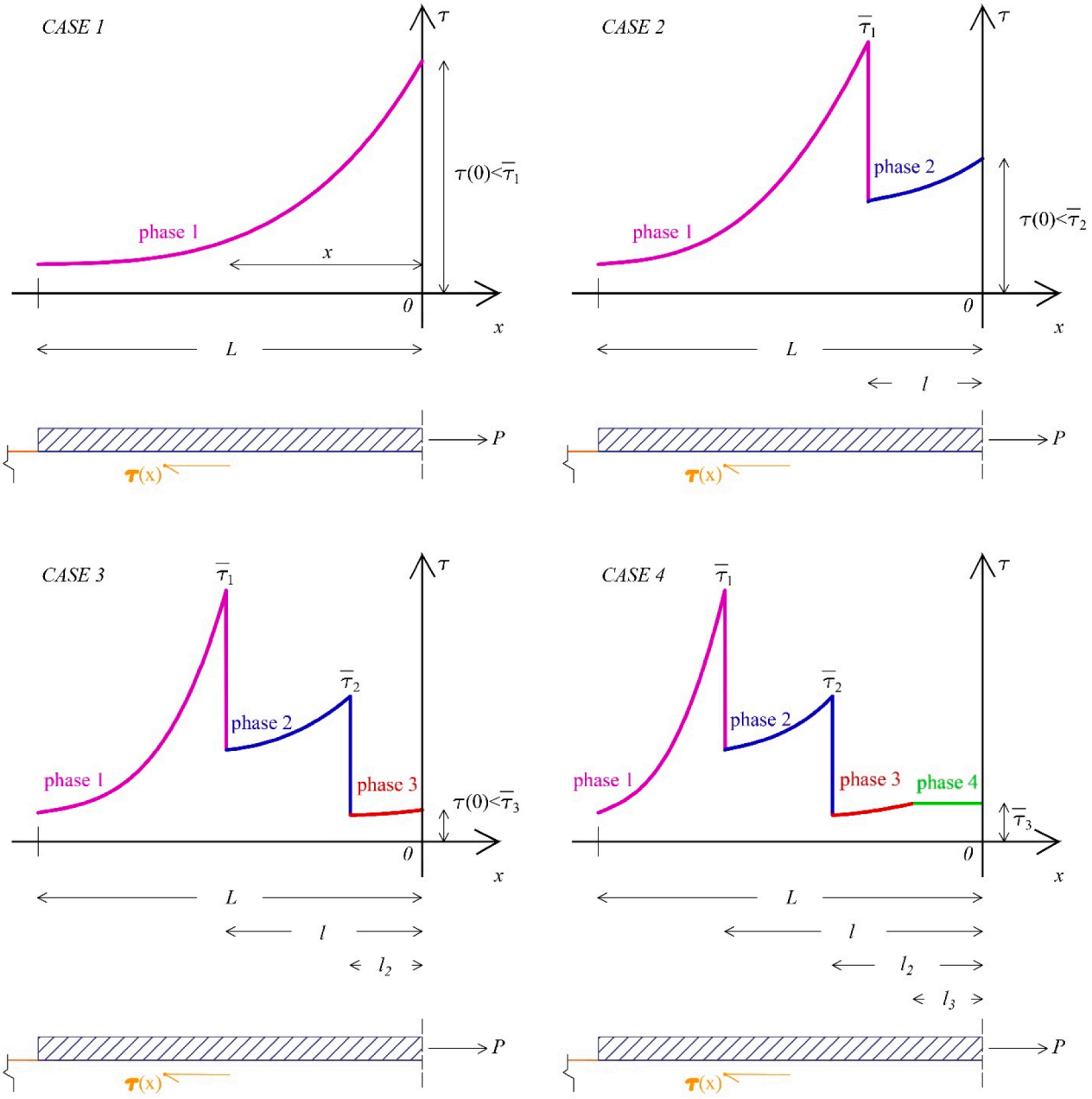


**Fig. 3.** Phases of the analytical model and corresponding shear stress shape along the bond length; meaning of $l$, $l_2$ and $l_3$.

-depending on the boundary conditions imposed at the free and loaded edge- either Runge-Kutta or finite difference BVP Boundary Value Problem solvers. Other advantages when comparing with the already existent trilinear model is that any softening law can be simulated and a commercial FE software equipped only with very simple non-linear elements (cutoff and elastic-perfectly plastic trusses) can be used to analyze any kind of test and reinforced structure strengthened with TRM, as discussed in what follows. The mechanical parameters to set the sawtooth curve are in principle six, namely 3 stresses ($\bar{\tau}_1, \bar{\tau}_2, \bar{\tau}_3$) and 3 slips ($\bar{s}_1, \bar{s}_2, \bar{s}_3$), see Fig. 2. However, $\bar{\tau}_1$, $\bar{s}_1$, $\bar{s}_3$ and $\bar{\tau}_3$ are identical to those used in the trilinear model, meaning that only two parameters ($\bar{\tau}_2$ and $\bar{s}_2$) should be calibrated to exactly reproduce the same macroscopic behavior obtained with the trilinear approach. Such matter will be discussed later in the paper. Here the main features of the mathematical model are discussed.

In particular, when the behavior of the interface is elastic, an analytical solution can be retrieved easily. Eq. (3) is classically re-written as follows:

$$\frac{d^2 s}{dx^2} - \lambda^2 s = 0 \tag{4}$$

where $\lambda$ is equal to the following expression:

$$\lambda = \sqrt{\frac{p_f k}{E_f A_f}} \tag{5}$$

and $k$ indicates the stiffness of the interface, assuming $\tau = ks$. According to Fig. 2, we denote with $k_i$ is the stiffness of the $i$-th phase, keeping in mind that $k_4 = 0$.

Field equation (4) admits the following solution:

$$s = C_1 e^{\lambda x} + C_2 e^{-\lambda x} \tag{6}$$

Where $C_1$ and $C_2$ are 2 integration constants to be determined imposing suitable boundary conditions on either slip or fiber normal

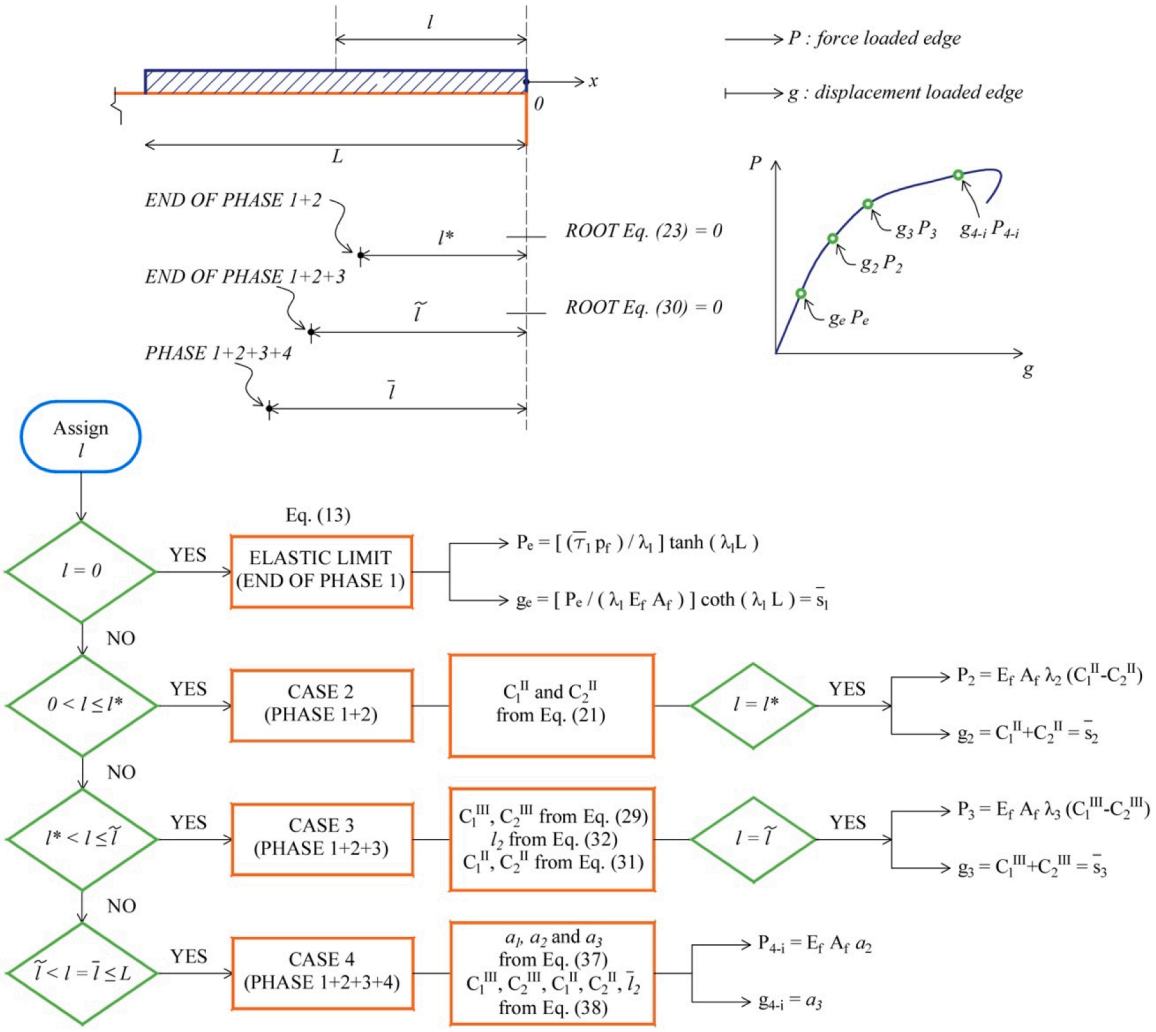


**Fig. 4.** Flowchart of the algorithm proposed to retrieve the global response.

stress.

Deriving (6), it is possible to deduce $\sigma$ as follows:

$$\sigma = E_f \frac{ds}{dx} = E_f \lambda \left( C_1 e^{\lambda x} - C_2 e^{-\lambda x} \right) \tag{7}$$

It is also worth mentioning that, from the field equation (3), $\tau$ is equal to the following expression:

$$\tau = \frac{E_f A_f}{p_f} \frac{d^2 s}{dx^2} - = \frac{E_f A_f}{p_f} \lambda^2 \left( C_1 e^{\lambda x} + C_2 e^{-\lambda x} \right) \tag{8}$$

As it can be noticed from the previous equations, $s$, $\sigma$ and $\tau$ exhibit an exponential shape along the bond length.

Fig. 3 depicts the shape of the tangential stress at the interface in the different phases (at the elastic limit and after the initial elastic phase) acting during the debonding process along the bonded length. As clearly understandable from Eq. (6), the shape is exponential. The following cases may occur, depending on the load applied externally:

- Case 1: only Phase 1 is active; the interface is elastic, the stiffness of the interface along the bond length is everywhere equal to $k_1$;
- Case 2: Phase 1 and Phase 2 are active contemporarily; the interface is always elastic, but the stiffness of the interface changes along the bonded length and is respectively equal to $k_1$ between $-L$ and $-l$, and equal to $k_2$ between $-l$ and 0;
- Case 3: Phase 1, 2 and 3 are active contemporarily; the interface is elastic per initial assumptions of the interface behavior and its stiffness changes three times along the bonded length. It is equal to the following values: $k_1$ between $-L$ and $-l$, $k_2$ between $-l$ and $-l_2$ and $k_3$ between $-l_2$ and 0.
- Case 4: Phase 1, 2, 3 and 4 are all active contemporarily; the interface is elastic -exception made for Phase 4-, and the stiffness of the interface changes four times along the length, being equal to $k_1$ between $-L$ and $-l$, to $k_2$ between $-l$ and $-l_2$, to $k_3$ between $-l_2$ and $-l_3$ and vanishing over $-l_3$ (in this last region the field equation will become non-homogeneous with separable variables).

Hereafter the analytical solution for the different cases previously introduced is discussed separately.

From here ongoing, we will indicate with $s_i$ and $\sigma_i$ the slip and the fiber normal stress functions in the $i$-th phase. $\lambda_i$ will be the constant defined in Eq. (5) when the interface stiffness is $k_i$, whereas with $C_{1,2}^R$ we will indicate the integration constants for Phase $R$ ($R$ Roman number).

The logical procedure followed to retrieve analytically the global response in terms of force applied $P$ vs displacement $g$ at the loaded edge is provided in the flowchart of Fig. 4.

As it is possible to notice, the only independent variable to set in input is the abscissa ($-l$) of the point where the interface leaves Phase 1 and enters in Phase 2; $-l$ should be varied between 0 (elastic limit, interface all in Phase 1) and $-L$ (interface all beyond Phase 1).

In what follows the different possible cases are discussed in detail.

**Case 1.** According to Fig. 1, and considering a $P$ force applied at the

**Table 1**
Parameters used for the validation of the sawtooth model.

| Label | $E_f$[MPa] | $A_f$[$mm^2$] | $p_f$[mm] | $L_b$[mm] | $\tau_1$[MPa] | $k_1$[MPa/mm] | $\lambda_1$[$mm^{-1}$] | $\tau_3$[MPa] | $k_3$[MPa/mm] | $\lambda_3$[$mm^{-1}$] |
|---|---|---|---|---|---|---|---|---|---|---|
| Tri-linear law* | 190,000 | 4.84 | 23.40 | 450 | 5.31 | 37.1 | 0.0097 | 0.52 | 1.06 | 0.0051 |

* data obtained from the experimental campaign carried out in Section 3

loaded edge, the boundary conditions to impose are the following:

$$\sigma_1 = E_f \left.\frac{ds_1}{dx}\right|_{x=-L} = 0 \tag{9}$$

$$\sigma_1 = E_f \left.\frac{ds_1}{dx}\right|_{x=0} = \frac{P}{A_f} \tag{10}$$

Such boundary conditions match exactly the experimental setup in a force control test.

With the previous boundary conditions the solution of equation (4) is the following:

$$s_1 = \frac{P}{\lambda_1 E_f A_f}\frac{\cosh[\lambda_1(L+x)]}{\sinh(\lambda_1 L)} \tag{11}$$

The elastic limit is attained when the tangential stress at the loaded edge is equal to $\bar{\tau}_1$, i.e. when the second derivative of the slip in the origin is equal to the following expression:

$$\left.\frac{d^2 s_1}{dx^2}\right|_{x=0} = \frac{p_f \bar{\tau}_1}{E_f A_f} \tag{12}$$

Which in turn allows to determine the force and the slip at the loaded edge at the elastic limit:

$$\begin{aligned} P_e &= \frac{\bar{\tau}_1 p_f}{\lambda_1}\tanh(\lambda_1 L) \\ g_e &= \frac{P_e}{\lambda_1 E_f A_f}\coth(\lambda_1 L) = \bar{s}_1 \end{aligned} \tag{13}$$

**Case 2.** When Phase 2 activates, the algorithm requires to set in input a value of $-l$ (identifying as already pointed out the transition point between Phase 1 and 2) ranging from $-L$ to $0$. Integration constants $C^I_{1,2}$ can be straightforwardly derived imposing the following boundary conditions:

$$\sigma_1|_{x=-L} = 0 \tag{14}$$

$$\frac{E_f A_f}{p_f}\left.\frac{d^2 s_1}{dx^2}\right|_{x=-l} = \bar{\tau}_1 \tag{15}$$

Such conditions allow writing the following system, Eq. (16), of two equations into two unknowns:

$$\begin{cases} E_f\left(C^I_1\lambda_1 e^{-\lambda_1 L} - C^I_2\lambda_1 e^{\lambda_1 L}\right) = 0 \\ \bar{\tau}_1 = \dfrac{E_f A_f}{p_f}\left(C^I_1\lambda_1^2 e^{-\lambda_1 l} + C^I_2\lambda_1^2 e^{\lambda_1 l}\right) \end{cases} \tag{16}$$

Which straightforwardly returns $C^I_1$, and $C^I_2$ constants:

$$\begin{aligned} C^I_1 &= \frac{\bar{\tau}_1 p_f}{E_f A_f}\frac{e^{\lambda_1 L}}{\lambda_1^2\left[e^{-\lambda_1(L-l)} + e^{\lambda_1(L-l)}\right]} \\ C^I_2 &= \frac{\bar{\tau}_1 p_f}{E_f A_f}\frac{e^{-\lambda_1 L}}{\lambda_1^2\left[e^{-\lambda_1(L-l)} + e^{\lambda_1(L-l)}\right]} \end{aligned} \tag{17}$$

Phase 2 integration constants $C^{II}_{1,2}$ are then determined in cascade assuming the continuity of both the slip and the fiber axial stress at $-l$:

$$\begin{aligned} &C^{II}_1 e^{-\lambda_2 l} + C^{II}_2 e^{\lambda_2 l} = C^I_1 e^{-\lambda_1 l} + C^I_2 e^{\lambda_1 l} = s_1(-l) \\ &\lambda_2\left(C^{II}_1 e^{-\lambda_2 l} - C^{II}_2 e^{\lambda_2 l}\right) = \lambda_1\left(C^I_1 e^{-\lambda_1 l} - C^I_2 e^{\lambda_1 l}\right) = \frac{\sigma_1(-l)}{E_f} \end{aligned} \tag{18}$$

Again $C^{II}_1$ and $C^{II}_2$ are deduced easily solving a system of two equations into two unknowns; they are equal to:

$$\begin{aligned} C^{II}_1 &= \frac{e^{\lambda_2 l}}{2}\left(s_1(-l) + \frac{\sigma_1(-l)}{\lambda_2 E_f}\right) \\ C^{II}_2 &= \frac{e^{-\lambda_2 l}}{2}\left(s_1(-l) - \frac{\sigma_1(-l)}{\lambda_2 E_f}\right) \end{aligned} \tag{19}$$

It is interesting to point out that at the transition point the following relations hold:

$$\begin{aligned} &s_1(-l) = \bar{s}_1 \\ &\sigma_1(-l) = \frac{\bar{\tau}_1 p_f}{\lambda_1 A_f}\frac{e^{\lambda_1(L-l)} - e^{-\lambda_1(L-l)}}{e^{\lambda_1(L-l)} + e^{-\lambda_1(L-l)}} = \frac{\bar{\tau}_1 p_f}{\lambda_1 A_f}\tanh[\lambda_1(L-l)] \end{aligned} \tag{20}$$

Combining Eqs. (19) and (20) we obtain:

$$\begin{aligned} C^{II}_1 &= \frac{e^{\lambda_2 l}}{2}\left(\bar{s}_1 + \frac{\bar{\tau}_1 p_f}{\lambda_1\lambda_2 E_f A_f}\frac{e^{\lambda_1(L-l)} - e^{-\lambda_1(L-l)}}{e^{\lambda_1(L-l)} + e^{-\lambda_1(L-l)}}\right) \\ C^{II}_2 &= \frac{e^{-\lambda_2 l}}{2}\left(\bar{s}_1 - \frac{\bar{\tau}_1 p_f}{\lambda_1\lambda_2 E_f A_f}\frac{e^{\lambda_1(L-l)} - e^{-\lambda_1(L-l)}}{e^{\lambda_1(L-l)} + e^{-\lambda_1(L-l)}}\right) \end{aligned} \tag{21}$$

Defining with $l^*$ that particular value of $l$ corresponding to the triggering of Phase 3 in the origin, then the following equality holds:

$$\begin{aligned} \bar{\tau}_2 &= \frac{E_f A_f}{p_f}\lambda_2^2\left(C^{II}_1 + C^{II}_2\right) \\ &= \frac{E_f A_f \lambda_2^2}{p_f}\left[\bar{s}_1\cosh(\lambda_2 l^*) + \frac{\bar{\tau}_1 p_f}{\lambda_1\lambda_2 E_f A_f}\tanh[\lambda_1(L-l^*)]\sinh(\lambda_2 l^*)\right] \end{aligned} \tag{22}$$

Let's define the function $y$ as follows:

$$y = \frac{E_f A_f \lambda_2^2}{p_f}\left[\bar{s}_1\cosh(\lambda_2 l^*) + \frac{\bar{\tau}_1 p_f}{\lambda_1\lambda_2 E_f A_f}\tanh[\lambda_1(L-l^*)]\sinh(\lambda_2 l^*)\right] - \tau_2 \tag{23}$$

the root of $y$ is easily found within a common spreadsheet, finding the minimum of $\ln|y|$. For the problem at hand, assuming the data of Table 1, the following values for $l^*$ are found:

- $l^* = 37.84$ mm for $\bar{\tau}_2 = 6.5$ MPa, $\bar{s}_2$=0.37 mm;
- $l^* = 39.03$ mm for $\bar{\tau}_2 = 5.6$ MPa, $\bar{s}_2$=0.40 mm;
- $l^* = 39.60$ mm for $\bar{\tau}_2 = 5.2$ MPa, $\bar{s}_2$=0.43 mm;

Table 1 parameters are those then used in the validation section of the model. It is worth mentioning that they are not derived directly from experimental data, but they are set taking as reference a trilinear law usually adopted in the literature to analytically and numerically analyze the FRCM debonding from a rigid support. In particular, $k_1 = \frac{\bar{\tau}_1}{\bar{s}_1}$, $k_3 = \frac{\bar{\tau}_3}{\bar{s}_3}$ (see Fig. 2 for the meaning of the symbols), whereas $\lambda_i = \sqrt{p_f k_i}/\sqrt{E_f A_f}$.

As far as the global behavior is concerned, the end of Phase 1 + 2 is characterized by the following applied force and slip at the loaded edge:

$$\begin{aligned} P_2 &= E_f A_f \lambda_2\left(C^{II}_1 - C^{II}_2\right) \\ g_2 &= C^{II}_1 + C^{II}_2 = \bar{s}_2 \end{aligned} \tag{24}$$

where $C^{II}_1$ and $C^{II}_2$ are evaluated keeping $l = l^*$.

**Case 3.** When $l > l^*$ Phase 3 triggers in correspondence of a further transition point located at $-l_2$.

At a given value of $l > l^*$, then $l_2$ can be determined in closed form remembering both that $C_{1,2}^{II}$ are known from Eq. (19) and that:

$$\overline{\tau}_2 = \frac{E_f A_f}{p_f}\lambda_2^2\left(C_1^{II}e^{-\lambda_2 l_2} + C_2^{II}e^{\lambda_2 l_2}\right) \tag{25}$$

With the position $X = e^{\lambda_2 l_2}$ the previous equation can be rearranged as follows:

$$\begin{aligned} &C_2^{II}X^2 - KX + C_1^{II} = 0 \\ &K = \frac{\overline{\tau}_2 p_f}{E_f A_f \lambda_2^2} \end{aligned} \tag{26}$$

Generally, for the cases of practical interest under consideration, the quadratic Eq. (26) admits two real solutions, only one of them of interest for the present computations -because positive-, which is:

$$X = \frac{K - \sqrt{K^2 - 4C_1^{II}C_2^{II}}}{2C_2^{II}} \tag{27}$$

The knowledge of $X$ from Eq. (27) allows the determination of $l_2$:

$$l_2 = \frac{\ln X}{\lambda_2} \tag{28}$$

Integration constants of Phase 3 are calculated in the same way done for Phase 2; Eq. (19) is indeed recursive (because two boundary conditions are imposed at the transition point) and constants $C_{1,2}^{III}$ are obtained as follows:

$$\begin{aligned} C_1^{III} &= \frac{e^{\lambda_3 l_2}}{2}\left[\overline{s}_2 + \frac{E_f\left(C_1^{II}\lambda_2 e^{-\lambda_2 l_2} - C_2^{II}\lambda_2 e^{\lambda_2 l_2}\right)}{\lambda_3 E_f}\right] \\ C_2^{III} &= \frac{e^{-\lambda_3 l_2}}{2}\left[\overline{s}_2 - \frac{E_f\left(C_1^{II}\lambda_2 e^{-\lambda_2 l_2} - C_2^{II}\lambda_2 e^{\lambda_2 l_2}\right)}{\lambda_3 E_f}\right] \end{aligned} \tag{29}$$

It is also interesting to evaluate that value of $l = \widetilde{l}$ that is responsible for the triggering of the last Phase 4 at the origin point.

In such condition, the origin exhibits a tangential stress at the interface equal to $\overline{\tau}_3$, namely the following equation holds:

$$z = \overline{\tau}_3 - \frac{E_f A_f}{p_f}\lambda_3^2\left(C_1^{III} + C_2^{III}\right) = 0$$

$$z = \overline{\tau}_3 - \frac{E_f A_f \lambda_3^2}{p_f}\left[\overline{s}_2\cosh(\lambda_3 l_2) + \left(\frac{C_1^{II}\lambda_2 e^{-\lambda_2 l_2}}{\lambda_3} - \frac{C_2^{II}\lambda_2 e^{\lambda_2 l_2}}{\lambda_3}\right)\sinh(\lambda_3 l_2)\right] = 0 \tag{30}$$

Under the assumptions that:

$$\begin{aligned} C_1^{II} &= \frac{e^{\lambda_2 \widetilde{l}}}{2}\left\{\overline{s}_1 + \frac{\overline{\tau}_1 p_f}{\lambda_1\lambda_2 E_f A_f}\tanh\left[\lambda_1\left(L - \widetilde{l}\right)\right]\right\} \\ C_2^{II} &= \frac{e^{-\lambda_2 \widetilde{l}}}{2}\left\{\overline{s}_1 - \frac{\overline{\tau}_1 p_f}{\lambda_1\lambda_2 E_f A_f}\tanh\left[\lambda_1\left(L - \widetilde{l}\right)\right]\right\} \end{aligned} \tag{31}$$

$$\begin{aligned} &K = \frac{\overline{\tau}_2 p_f}{E_f A_f \lambda_2^2} \\ &X = \frac{K - \sqrt{K^2 - 4C_1^{II}C_2^{II}}}{2C_2^{II}} \\ &l_2 = \frac{\ln X}{2\lambda_2} \end{aligned} \tag{32}$$

The root of equation (30) is determined numerically (again by means of a commercial spreadsheet) in the same way used for $l^*$, allowing the identification of that value of $l = \widetilde{l}$ that activates the fourth and last phase at the origin. Let's also indicate with $\widetilde{l}_2$ the transition point between Phase 1 and 2 for $l = \widetilde{l}$.

At the end of Phase 1 + 2 + 3, the loaded edge applied force and slip are the following:

$$\begin{aligned} P_3 &= E_f A_f \lambda_3\left(C_1^{III} - C_2^{III}\right) \\ g_3 &= C_1^{III} + C_2^{III} = \overline{s}_3 \end{aligned} \tag{33}$$

**Case 4.** When $l > \widetilde{l}$, the last portion of the interface near the loaded end is in Phase 4. There, $\lambda_4 = 0$, $\overline{\tau}_3$ is constant, $-l_3$ identifies the position where Phase 4 begins, and the corresponding field differential equation becomes nonhomogeneous with separable variables:

$$\frac{d^2 s_4}{dx^2} = \frac{p_f \overline{\tau}_3}{E_f A_f} \tag{34}$$

$s_4$ is clearly parabolic and can be written as follows:

$$s_4 = a_1 x^2 + a_2 x + a_3 \tag{35}$$

where $a_1$, $a_2$ and $a_3$ are integration constants. They are determined imposing at $-l_3$ the following conditions:

$$\begin{cases} \overline{s}_3 = a_1 l_3^2 - a_2 l_3 + a_3 \\ C_1^{III}\lambda_3 e^{-\lambda_3 l_3} - C_2^{III}\lambda_3 e^{\lambda_3 l_3} = -2a_1 l_3 + a_2 \\ \dfrac{p_f \overline{\tau}_3}{E_f A_f} = 2a_1 \end{cases} \tag{36}$$

The linear system of equations (36) provides immediately the integration constants by triangular substitution:

$$\begin{cases} a_1 = \dfrac{1}{2}\dfrac{p_f \overline{\tau}_3}{E_f A_f} \\ a_2 = C_1^{III}\lambda_3 e^{-\lambda_3 l_3} - C_2^{III}\lambda_3 e^{\lambda_3 l_3} + 2a_1 l_3 \\ a_3 = \overline{s}_3 - a_1 l_3^2 + a_2 l_3 \end{cases} \tag{37}$$

In this case, it is necessary to evaluate $l_3$, which identifies the transition point between Phase 3 and 4.

Let us pose $l = \overline{l} > \widetilde{l}$, indicating the transition point between Phase 1 and 2, whereas $\overline{l}_2$ is the transition point between Phase 2 and 3.

In such situation the following relations hold:

$$\begin{cases} C_1^{I} = \dfrac{\overline{\tau}_1 p_f}{E_f A_f}\dfrac{e^{\lambda_1 L}}{\lambda_1^2\left[e^{-\lambda_1(L-\overline{l})} + e^{\lambda_1(L-\overline{l})}\right]} \\ C_2^{I} = \dfrac{\overline{\tau}_1 p_f}{E_f A_f}\dfrac{e^{-\lambda_1 L}}{\lambda_1^2\left[e^{-\lambda_1(L-\overline{l})} + e^{\lambda_1(L-\overline{l})}\right]} \\ C_1^{II} = \dfrac{e^{\lambda_2 \overline{l}}}{2}\left\{\overline{s}_1 + \dfrac{\overline{\tau}_1 p_f}{\lambda_1\lambda_2 E_f A_f}\tanh[\lambda_1(L-\overline{l})]\right\} \\ C_2^{II} = \dfrac{e^{-\lambda_2 \overline{l}}}{2}\left\{\overline{s}_1 - \dfrac{\overline{\tau}_1 p_f}{\lambda_1\lambda_2 E_f A_f}\tanh[\lambda_1(L-\overline{l})]\right\} \\ X = \dfrac{K - \sqrt{K^2 - 4C_1^{II}C_2^{II}}}{2C_2^{II}} \\ \overline{l}_2 = \dfrac{\ln X}{\lambda_2} \\ C_1^{III} = \dfrac{e^{\lambda_3 \overline{l}_2}}{2}\left[\overline{s}_2 + \dfrac{E_f\left(C_1^{II}\lambda_2 e^{-\lambda_2 \overline{l}_2} - C_2^{II}\lambda_2 e^{\lambda_2 \overline{l}_2}\right)}{\lambda_3 E_f}\right] \\ C_2^{III} = \dfrac{e^{-\lambda_3 \overline{l}_2}}{2}\left[\overline{s}_2 - \dfrac{E_f\left(C_1^{II}\lambda_2 e^{-\lambda_2 \overline{l}_2} - C_2^{II}\lambda_2 e^{\lambda_2 \overline{l}_2}\right)}{\lambda_3 E_f}\right] \end{cases} \tag{38}$$

The transition point $\overline{l}_3$ between Phase 3 and 4 is found using exactly

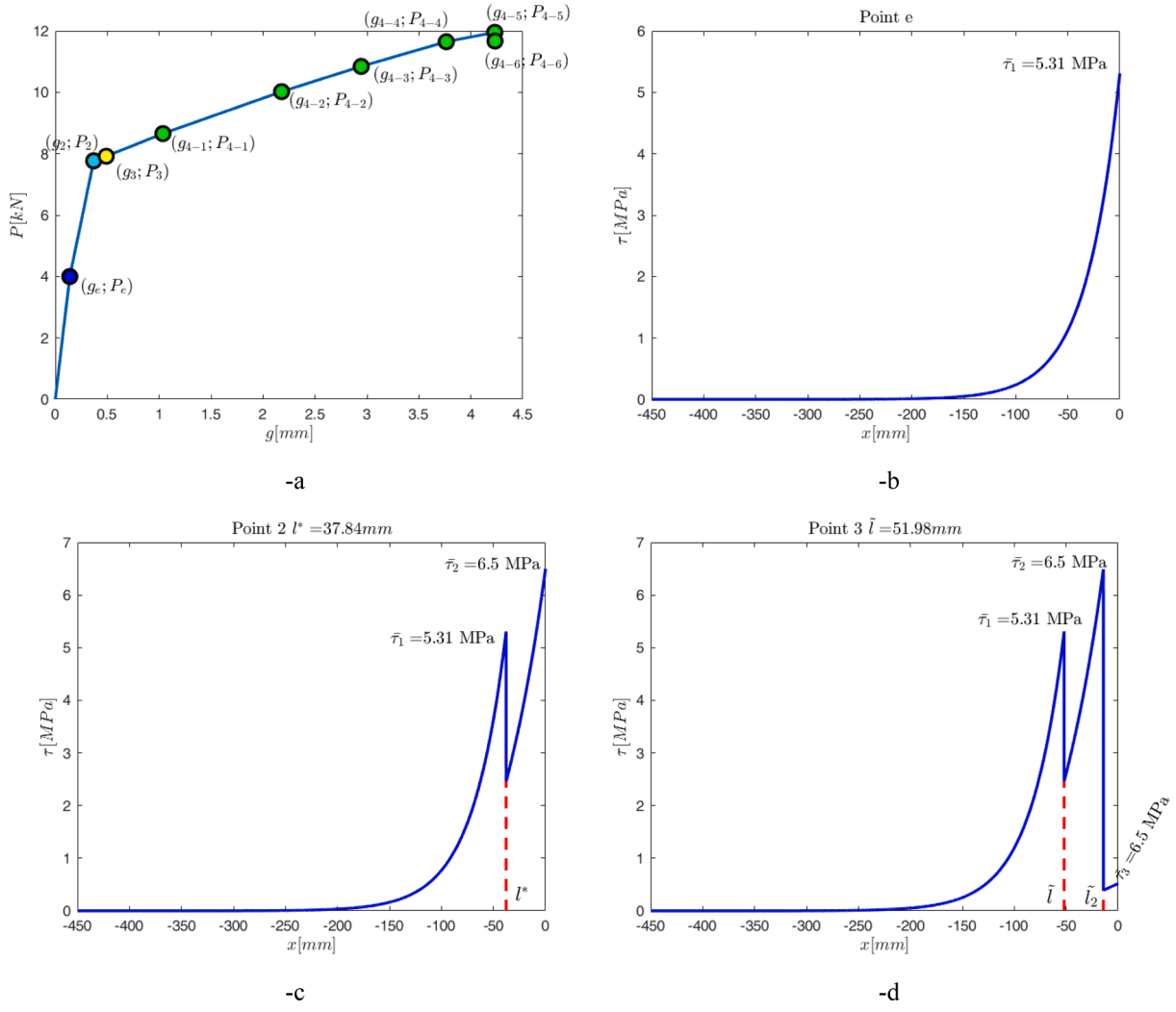


**Fig. 5.** Analytical force-slip curve (-a) and distribution of tangential stresses at the interface along the bonded length in correspondence of Point *e* (-b), Point 2 (-c) and Point 3 (-d).

the same procedure adopted for $\bar{l}_2$, namely:

$$\begin{cases} w = \bar{\tau}_3 - \dfrac{E_f A_f}{p_f}\lambda_3^2\left(C_1^{III} e^{-\lambda_3 l_3} + C_2^{III} e^{-\lambda_3 l_3}\right) = 0 \\ K_2 = \dfrac{\bar{\tau}_3 p_f}{E_f A_f \lambda_3^2} \\ X_2 = \dfrac{K_2 - \sqrt{K_2^2 - 4C_1^{III} C_2^{III}}}{2C_2^{III}} \\ \bar{l}_3 = \dfrac{\ln X_2}{\lambda_3} \end{cases} \tag{39}$$

As far as the force–displacement curve is concerned, the slip and the force at the loaded edge (origin) are the following:

$$\begin{aligned} P_{4-i} &= E_f A_f a_2 \\ g_{4-i} &= a_3 \end{aligned} \tag{40}$$

The subscript $i$ in the previous Eq. (40) indicates that quantities are estimated at a specific value of $l$ chosen at user's discretion.

To summarize, beyond the elastic limit, the algorithm proceeds at assigned values of $l$, and the following basic quantities are computed:

- Elastic limit (attainment of $\bar{\tau}_1$ in the origin); global quantities -slip and applied force at the loaded edge- are $g_e$ and $P_e$ respectively.
- $l^*$ (value of $l$ where in the origin $\bar{\tau}_2$ is attained); global quantities -slip and applied force at the loaded edge- are $g_2$ and $P_2$ respectively.
- $\tilde{l}$ (value of $l$ where in the origin $\bar{\tau}_3$ is attained) and $\tilde{l}_2$ (transition point between Phase 1 and 2 for $l = \tilde{l}$); global quantities -slip and applied force at the loaded edge- are $g_3$ and $P_3$ respectively.
- $\tilde{l} < \bar{l} < L$ (more than one value can be easily investigated), $\bar{l}_2$ (transition point between Phase 2 and 3) and $\bar{l}_3$ (transition point between Phase 3 and 4); global quantities -slip and applied force at the loaded edge- are $g_{4-i}$ and $P_{4-i}$ respectively.

For illustrative purposes, assuming $\bar{\tau}_2 = 6.5$ MPa and $\bar{s}_2 = 0.37$ mm, with the other quantities kept equal to those reported in Table 1, in Fig. 5 the global behavior of the specimen is shown, with the distribution of the tangential stresses along the bonded length for points *e*, 2 and 3. It is particularly evident how the peaks of the stress on the interface move rapidly from the loaded edge to the middle of the specimen. After Point 3, it should be noted how the pseudo-linear hardening behavior observed in the force-slip curves in correspondence of points $4-i$ is a consequence of the assumption of a non-zero tangential stress in Phase 4. In Fig. 6, the distribution of tangential stresses along the bonded length in 6 instants of the loading process when Phase 4 is fully developed are depicted. As can be seen, there is a progressive translation of the debonded area from the right (loaded edge) to the left (free edge) until

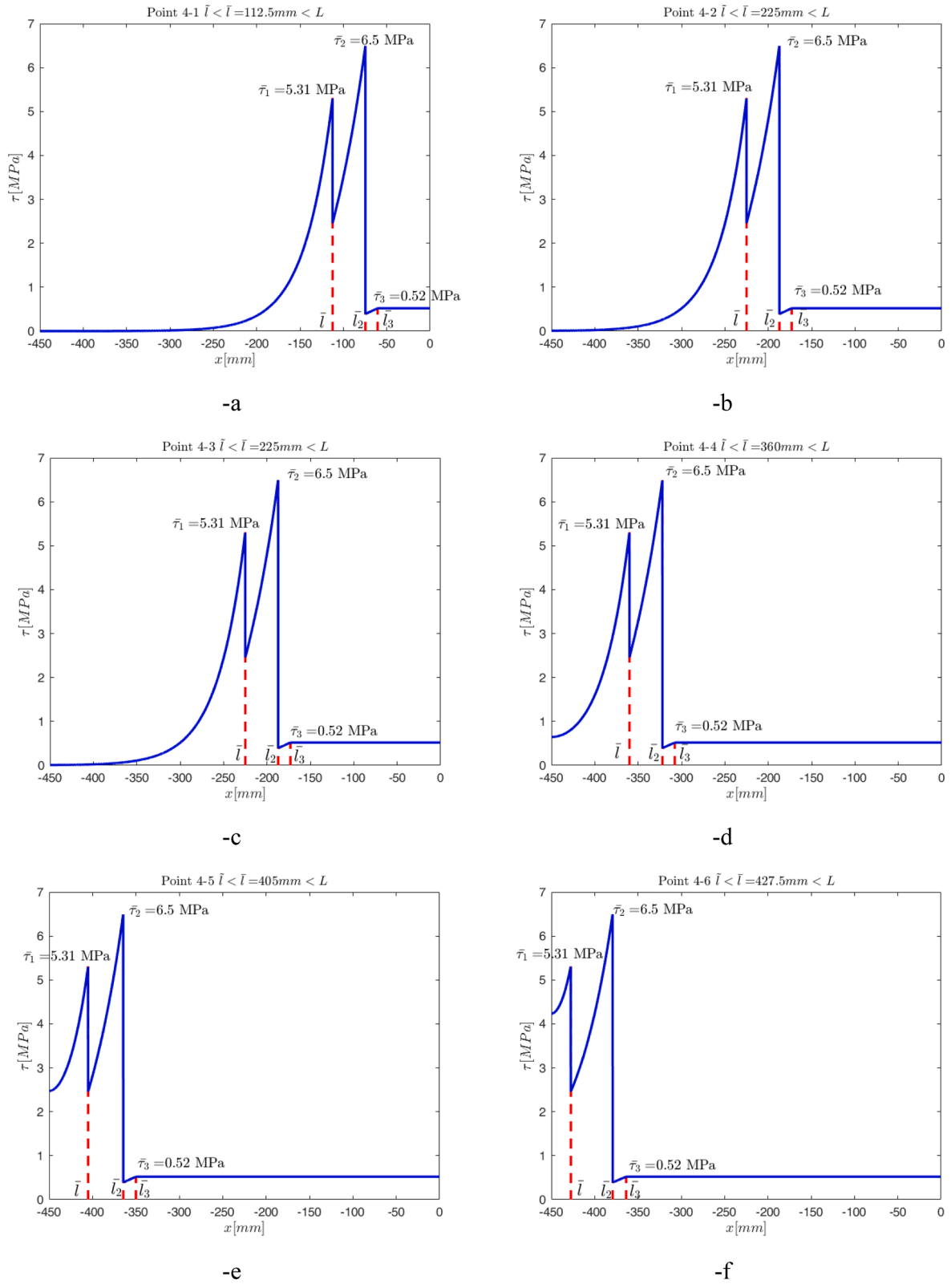


**Fig. 6.** Distribution of tangential stresses at the interface along the bonded length with Phase 4 fully developed. From -a to -f: Points from 4 to 1 to 4–6.

the failure of the specimen is reached.

Finally, it is important to point out that the analytical procedure allows also to depict the full debonding curve and not only the response at Points *e*, 1, 2, 3 and 4-*i*, simply repeating the calculations at a desired value of $l$ selected in input.

### 2.2. Implementation of the proposed model in a commercial FE code

As already pointed out, the advantage of utilizing a sawtooth $\tau(x)$ - $s(x)$ interface law stands in the possibility of its direct implementation in a FE commercial code equipped with trusses exhibiting a linear elastic and either perfect fragile (cutoff bar brittle) or perfectly plastic (cutoff

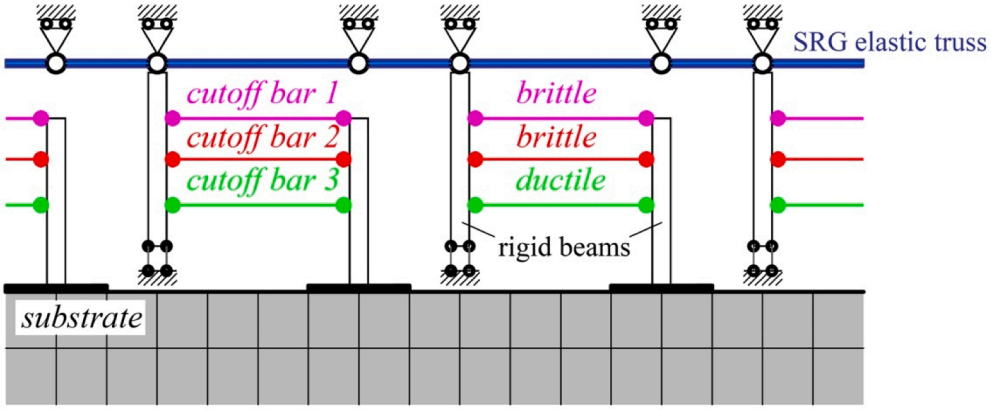


**Fig. 7.** sawtooth interface model implemented in a standard commercial FE code using cutoff bars disposed in-parallel (two brittle and one ductile).

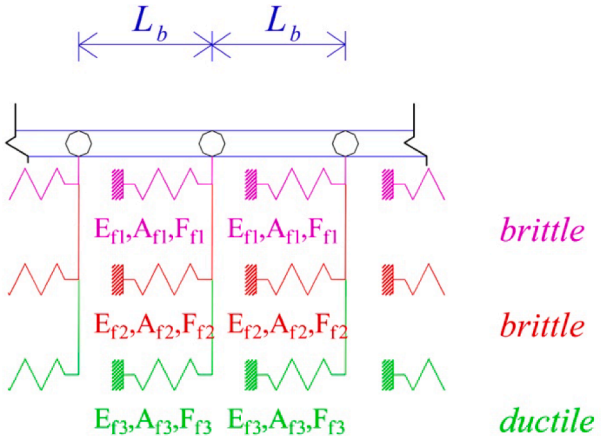


**Fig. 8.** One-dimensional FE model with 2 brittle and 1 ductile cutoff bars applied in parallel to the SRG nodes.

bar ductile) behavior. Such typology of FE is the simplest one among the big variety of existent elements usually available and nowadays is put at disposal to users in the most widespread commercial software, at the same time allowing fast and robust non-linear simulations and requiring a very basic theoretical background for the practitioner interested in performing non-linear structural analyses in presence of SRG/TRM reinforcement. The implementation proposed here and schematized in Fig. 7 does not require to write ad hoc subroutines, but needs only a specifically crafted discretization of the reinforcing system.

The mesh relies into three cutoff bars of finite length (established by the user), disposed in parallel and connected transversally with the support and the elastic SRG layer by means of rigid beams and suitable node constraints, as detailed in Fig. 7. Numerical simulations can be performed to both structural elements and entire structures.

According to Fig. 8, let $L_b$ be the length of the bars and let represent them with 3 springs applied to each node of the elastic reinforcement; $A_{fi}$, $E_{fi}$ and $F_{fi}$ indicate respectively the area, the elastic modulus and the ultimate tensile force of the $i$-th spring. Springs #1 and #2 exhibit an elastic perfectly brittle behavior, whereas spring #3 an elastic perfectly ductile behavior.

The equivalent elastic moduli of the springs, once that $A_{fi}$ is set equal to the unitary value for the sake of convenience, are calculated according to the following Eq. (41), assuming that the FE model and the sawtooth interface model exhibit the same slip at the node under consideration:

$$\begin{cases} E_{f1}A_{f1} + E_{f2}A_{f2} + E_{f3}A_{f3} = k_1 p_f {L_b}^2 \\ E_{f2}A_{f2} + E_{f3}A_{f3} = k_2 p_f {L_b}^2 \\ E_{f3}A_{f3} = k_2 p_f {L_b}^2 \end{cases} \tag{41}$$

Eq. (41) is an upper triangular linear system that furnishes immediately the values of $E_{fi}$ to adopt in the FE model, noting that $A_{fi}$ is unitary.

The ultimate resistances $F_{fi}$ of the 3 springs are calculated writing a system of 3 equilibrium equations into 3 unknows in correspondence of the end of Phase 1, Phase 2 and Phase 3; such system of equations is reported in the following Eq. (42):

$$\begin{cases} F_{f1} + F_{f2}\dfrac{\bar{s}_1}{\bar{s}_2} + F_{f3}\dfrac{\bar{s}_1}{\bar{s}_3} = \bar{\tau}_1 p_f L_b \\ F_{f2} + F_{f3}\dfrac{\bar{s}_2}{\bar{s}_3} = \bar{\tau}_2 p_f L_b \\ F_{f3} = \bar{\tau}_3 p_f L_b \end{cases} \tag{42}$$

## 3. In house experimentation: Single-lap direct shear experimental tests

The validation of the numerical model proposed is obtained making reference to a specific in-house experimentation carried out by the authors for this purpose. It is indeed always better to refer to experimental data obtained directly instead of using literature ones, simply because any needed mechanical and geometrical property can be retrieved without making arbitrary assumptions on the missing data, if any, as it may occur trying a validation using literature experimental data.

Hereafter, method, procedure and results of five direct-shear tests conducted to investigate the bond behavior of SRG-concrete joints subjected to a pure Mode-II loading condition are reported.

Few additional words should be spent as far as the hypothesis of a pure Mode-II loading condition is concerned. In fact, the suitability of the direct-shear test setup for the study of the Mode-II fracture mechanics behavior of bonded joints, including both FRP and FRCM (or TRM), has been widely examined in the scientific literature and is confirmed by experimental, numerical and analytical predictions. Some among the most relevant studies confirming this position are provided at [11,40-43]. In these studies, it is generally acknowledged that the cohesive interface of direct shear test specimens can be assumed to be subjected to a pure fracture mechanics Mode-II loading condition, although negligible stress components normal to the interface can arise due to the substrate bending effect induced by the eccentricity between the forces applied to the bonded strips and substrate.

Tests were performed with close reference to the indications of the European Assessment Document [44], which regulates the qualification of Inorganic Matrix Composites (IMC) systems for externally bonded

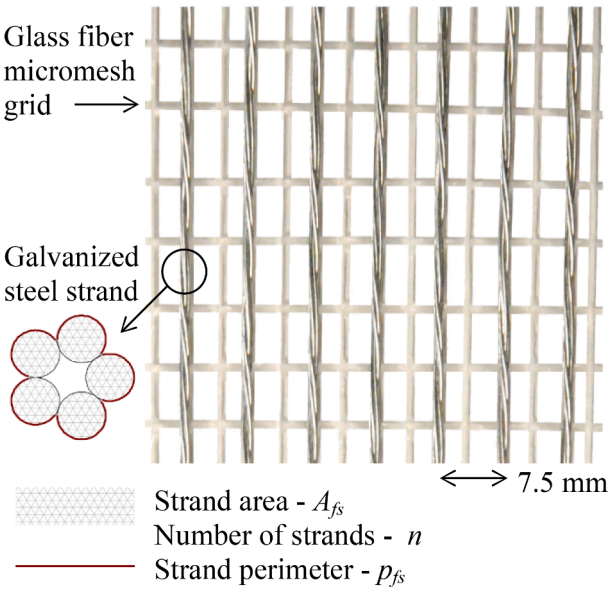


**Fig. 9.** textile grids geometry: steel.

applications. A classical push–pull configuration was adopted for the tests.

### 3.1. Materials

The SRG reinforcing pack investigated in this study relies on a unidirectional galvanized high-strength steel fiber textile [45] embedded with a geopolymer mortar [46]. Datasheets by the manufacturers [45,46] are used to set constituent materials properties (e.g. elastic moduli and resistances, area and perimeter of the steel fiber textile). Some experimental tests were also performed to validate the mechanical properties declared by the manufacturer. The obtained results confirmed the indicated mechanical properties. Fig. 9 shows the geometry of the steel textile, constituted by unidirectional twisted strands, spaced at 7.5 mm on center, held together by a glass fiber micromesh stable grid. Each strand has an area $A_{fs} = 0.538$ mm$^2$ and a perimeter $p_{fs} = 2.60$ mm (see Fig. 9), realized with 5 filaments, 3 straight and the remaining 2 twisted around the others. The tensile strength $f_f$ and elastic modulus $E_f$ of the steel textile are equal to 3000 MPa and 190 GPa, respectively, as declared by the manufacturer. The geopolymer mortar exhibits, again according to manufacturer data, a compressive strength ($R_{c28}$) of 50 MPa (after 28 days curing).

The composite system tested in direct shear tests is constituted by a single layer of textile embedded within two 5 mm thick layers of matrix, entailing an overall composite thickness of 10 mm. The composite strip was bonded to a concrete substrate having average compressive strength of 37.9 MPa (coefficient of variation, CoV, equal to 6.02%), determined by testing six 150 mm -edge cubes after 28 curing days [47]. The 28-days average tensile strength of concrete, obtained from splitting tests of five 100 mm × 200 mm cylinders, is 2.50 MPa (CoV = 18.40%) [48]. The direct shear tests were executed after more than one year from the substrate prisms casting.

### 3.2. Experimental set-up

The SRG-substrate joints were tested using a single-lap direct-shear test setup according to [44]. Specimens are constituted by a 10 mm thick rectangular composite strip of dimensions 450 × 60 mm with 9 strands embedded in a matrix, and bonded to a concrete prism with dimensions 150 × 150 mm (cross-section) × 600 mm (length). In agreement with the indications provided by the European Assessment Document for inorganic matrix composite systems qualification – Annex C.3 [44], prior the application of the composite strip, the substrate was roughened using a grinder and then thoroughly cleaned from dust with compressed

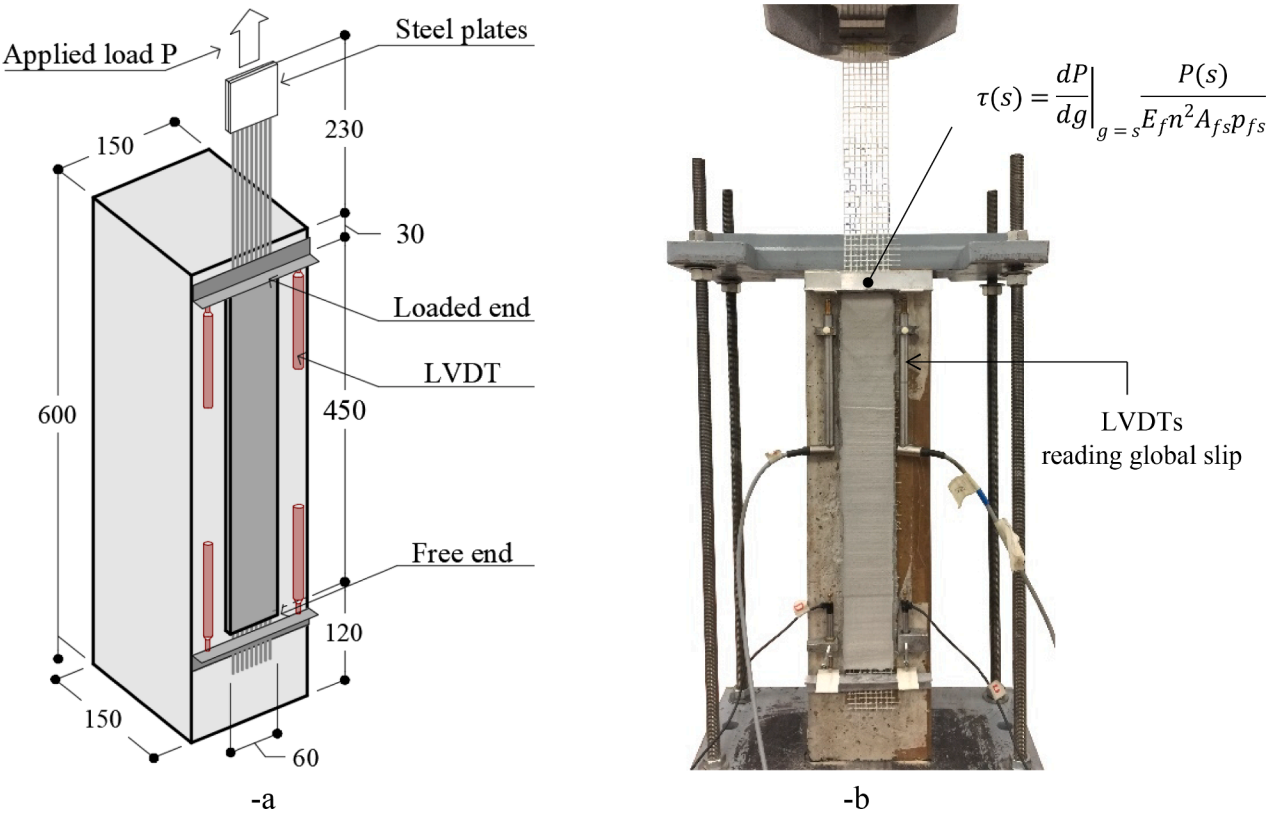


**Fig. 10.** -a: specimen geometry (dimensions in mm); -b: test setup.

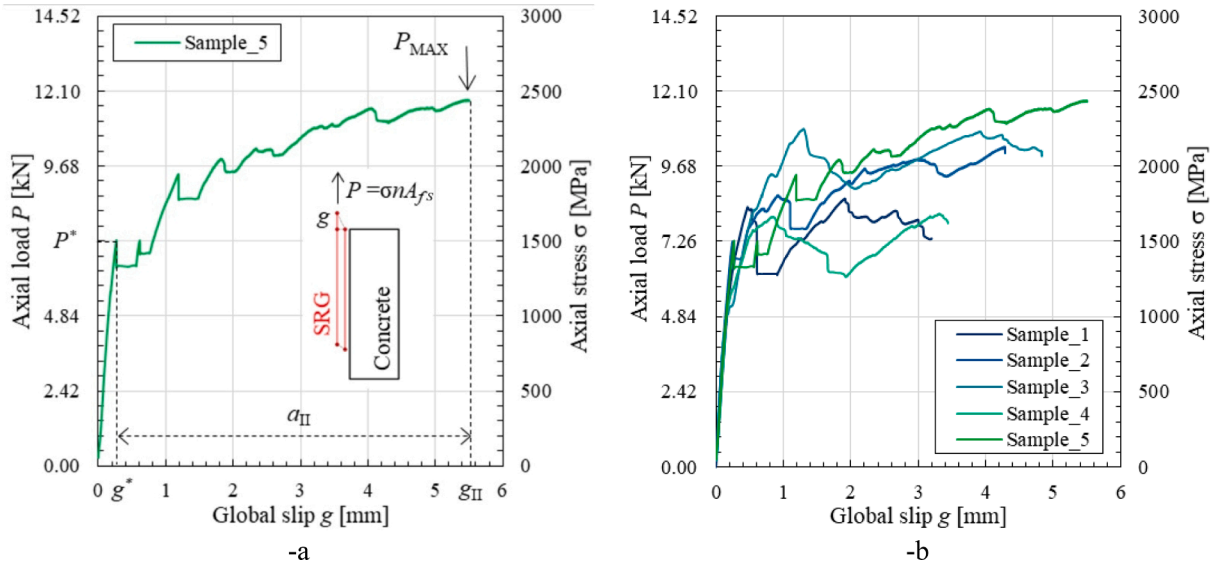


**Fig. 11.** Axial load (or stress), $P$ (or σ) - global slip, $g$, curves of SRG specimens: a) Typical $P$-$g$ behavior; b) all specimens.

air. Additionally, the substrate was wet using water few minutes before the application. Accordingly, specimens were prepared with close reference to the indications provided in the technical datasheet of the product [45,46], which is the same procedure that should be ideally followed in real applications. A first matrix layer was applied directly to the block surface using rectangular formworks, which allowed to maintain a constant thickness of 5 mm for the layer. The textile grid was then embedded on the matrix layer and pushed against it to guarantee good impregnation. Finally, the second matrix layer was applied, and the strip was cured 28 days in a 90% controlled humidity environment.

Fig. 10-a shows the specimen geometry and dimensions. As visible from Fig. 10-a, bare textile portions were left unembedded outside the composite strip beyond the loaded and free end positions. L-shaped aluminum plates were then attached to the bare textile just outside the composite strip ends to allow a direct measurement of the fiber–matrix relative slippage throughout the test. The displacements of the L-shaped plates with respect to the concrete prisms were measured by 4 LVDTs attached to the concrete substrate on the side of the composite strip. These were located at the loaded and at the free ends (see Fig. 10). The strip loaded end (Fig. 10-a) was located 30 mm apart from the prism edge to prevent the edge rupture.

The substrate block was restrained to the testing machine using a frame made of steel plates and bolted steel bars, according to the indications provided in [44], as shown in Fig. 10-b. The frame did not exhibit meaningful deformability and therefore it can be considered reasonably rigid. A MTS servo-hydraulic universal testing machine, equipped with a 250 kN load cell (resolution 0.005 kN) was adopted for the tests. Tests were performed in displacement control mode at a constant stroke rate of 0.2 mm/min, while the applied load was recorded by a 250 kN load cell. Thin steel plates were attached to the bare textile end using epoxy resin, to promote an effective and uniform machine gripping (see Fig. 10-a). Four HBM LVDT sensors were used to measure the relative displacement between the composite loaded and the concrete support, two of them having a 20 mm gauge length (resolution 0.001 mm, placed at the loaded end – see Fig. 10) and two having a 10 mm gauge length (resolution 0.0005 mm, placed at the free end – see Fig. 10).

### 3.3. Results

Fig. 11-a show the typical axial load (or stress) $P$ (or $\sigma$) - global slip $g$ response of the SRG-concrete joints, whereas the $P$ (or $\sigma$) - $g$ responses of all the tested specimens are collected in Fig. 11-b. In Fig. 11, $g$ is the

**Table 2**
Experimental test results of SRG strenghtened specimens: $P$-$g$ response parameters.

| Specimen name | $P^*$ [kN] | $g^*$ [mm] | $P_{MAX}$ [kN] | $a_{II}$ [mm] | $g_{II}$ [mm] | FAILURE MODE |
|---|---|---|---|---|---|---|
| Sample_1 | 8.375 | 0.47 | 8.650 | 2.73 | 3.20 | D + S |
| Sample_2 | 7.264 | 0.24 | 10.318 | 4.04 | 4.29 | D |
| Sample_3 | 10.894 | 1.30 | 10.896 | 3.53 | 4.83 | D |
| Sample_4 | 8.061 | 0.85 | 8.154 | 2.59 | 3.44 | D + S |
| Sample_5 | 7.285 | 0.27 | 11.809 | 5.24 | 5.51 | D |

Note: D = matrix-fiber interface debonding; D + S = matrix-fiber interface debonding combined with substrate debonding.

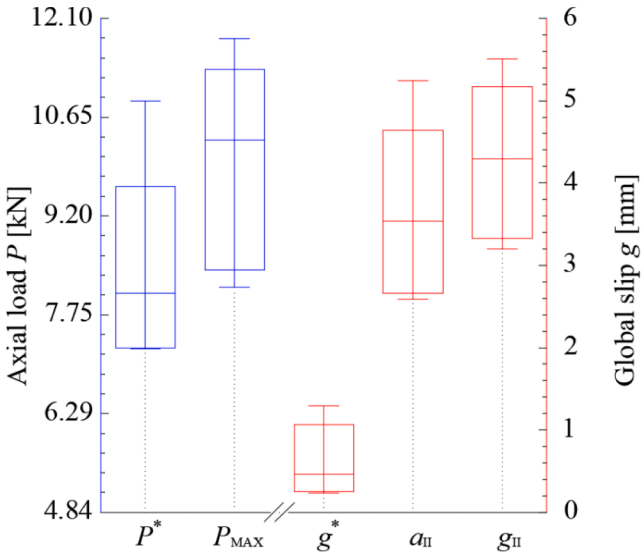


**Fig. 12.** Box-plot of the representative $P$-$g$ response parameters. On each box, the central mark indicates the median, the bottom and top edges of the box indicate the 25th and 75th percentiles, respectively.

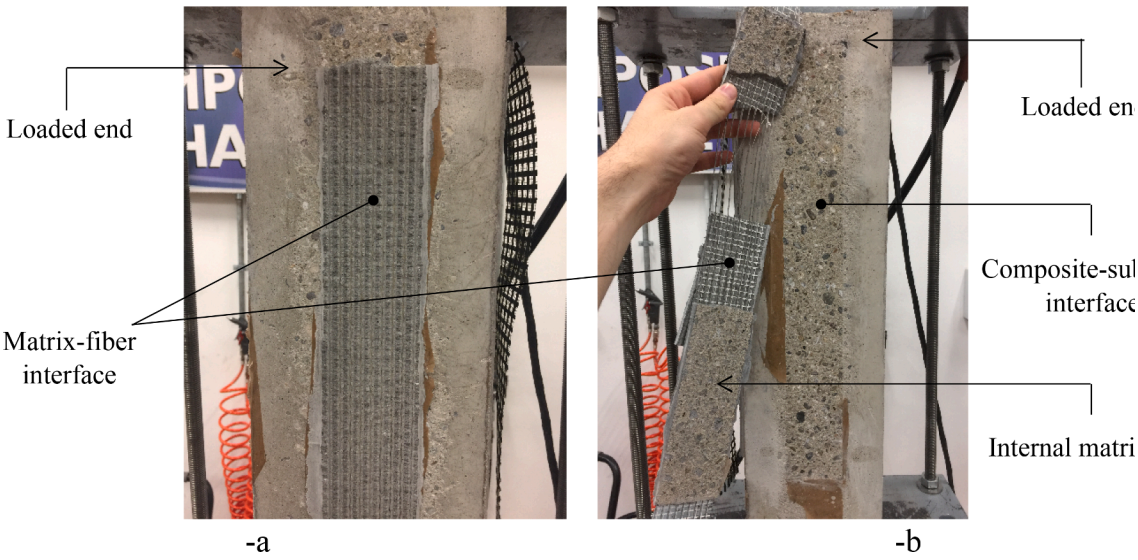


**Fig. 13.** Failure modes observed for the tested SRG-strengthened specimens: -a: debonding at the matrix-fiber interface with splitting of the matrix external layer from the internal one; -b: debonding of the matrix internal layer from the substrate.

average of the two LVDT readings at the loaded end and $\sigma$ is computed according to the equation:

$$\sigma = \frac{P}{nA_{fs}} \tag{43}$$

where $n$ and $A_{fs}$ are the number of fiber strands and the corresponding transversal area, respectively. Key parameters obtained from direct shear tests are reported in Table 2. Such parameters include the axial load at the end of the initial ascending branch $P^*$ and the corresponding global slip $g^*$, the maximum load recorded during the test $P_{MAX}$, the amplitude of the sub-horizontal branch, $a_{II}$ and the global slip at failure, $g_{II}$ (see Fig. 11-a). A box-plot with medians and quartiles, along with numerical predictions (discussed in the following sections) of the representative $P$-$g$ response parameters is reported in Fig. 12.

All SRG-strengthened specimens failed due to debonding at the matrix-fiber interface (see Fig. 5-a) with splitting of the matrix external layer from the internal one. In some cases, indicated with D + S in Table 2, debonding at the matrix-fiber interface was followed by the partial or total debonding of the matrix internal layer from the substrate (see Fig. 5-b). However, the matrix detachment from the substrate occurred suddenly in the very final stage of the test, as a consequence of the matrix-fiber interface failure. A similar failure mode was observed by Santandrea et al [49] in SRG-masonry joints subjected to a same test configuration.

The typical $P$ - $g$ response was characterized by two main stages, an ascending branch and a subsequent horizontal or slightly increasing branch (Fig. 11-a). The ascending branch observed was initially linear due to the elastic behavior of composite and substrate. When the bond strength of the matrix-fiber interface was attained at the loaded end, softening started propagating along the interface in the portion closer to the loaded end, and the load response became non-linear. Simultaneously, some orthogonal cracks (i.e. normal to the load direction) opened along the composite strip. However, due to the strong interlocking between textile and matrix, the loss of linearity associated with the interface softening was limited and small relative slippage between matrix and fiber was recorded in this stage. Increasing further the imposed displacement, the tangential stress transferred between matrix and fiber resulted in the formation of a main cohesive crack at the matrix-fiber interface, which corresponded to a sudden load drop in the $P$ - $g$ response. In some cases, the load reduction corresponding to the interfacial crack formation was less abrupt, because of a more even load distribution along the composite width. The load value attained at the end of the ascending branch is referred to as $P^*$ in Fig. 11-a, and the corresponding global slip is $g^*$. The opening of the interfacial crack determined the shifting from the first branch to the second sub horizontal or slightly ascending branch, which was associated with the propagation of the interfacial cohesive crack from the loaded end towards the free end of the specimen. As inferred in [49], where a comparison between load responses of specimens with different bonded lengths is reported, the amplitude of this second stage ($a_{II}$, see Fig. 11-a) depends mainly on the length of the bonded portion and turns out to be higher for joints with longer bonded lengths. During this stage, an increase of the applied load was recorded, which can be attributed to the friction exchanged between fiber and matrix and along the interfacial crack surface. This led to the attainment of the specimen bond capacity, referred to as $P_{MAX}$ in Fig. 11-a, which either occurred within or at the end of the second stage. This stage ended suddenly once debonding occurred at the matrix fiber interface and its amplitude, $a_{II}$ in Fig. 11-a, depended on the extent of the interfacial crack propagation. The global slip corresponding with failure was indicated with $g_{II}$. As shown in Fig. 13-b, for some specimens the presence of peeling stress (i.e. orthogonal to the composite plane) at the end of the test determined the local or total detachment of the composite strip from the substrate. In no cases free end slip reading was recorded due to the strong interlocking between fiber and matrix which prevented steel strands from slipping within the embedding matrix in the portion closer to the free end.

According to data represented in Fig. 12, a large scatter can be observed in the results of all tested specimens. A similar behavior was described by Santandrea et al. [49] testing SRG-masonry joints, a feature which was attributed to the variability of the inorganic matrix property and to its poor capability to impregnate steel strands.

### 3.4. Bond-slip behavior

The bond behaviour of SRG-strengthened specimens exhibiting a cohesive failure at the matrix-fiber interface can be analyzed through a fracture mechanics approach, by defining a specific relationship between the shear stress (i.e. bond stress) acting on the cohesive interface, $\tau$, and the relative sliding (or slip), $s$, between the two adherends, namely fiber and matrix. The $\tau(s)$ law of the cohesive interface, also referred to as Cohesive Material Law (CML), can be experimentally estimated on the result of bond tests. In [50], the CML of Carbon FRCM-masonry joints subjected to direct shear test and exhibiting a cohesive debonding at the matrix-fiber interface was experimentally estimated via direct

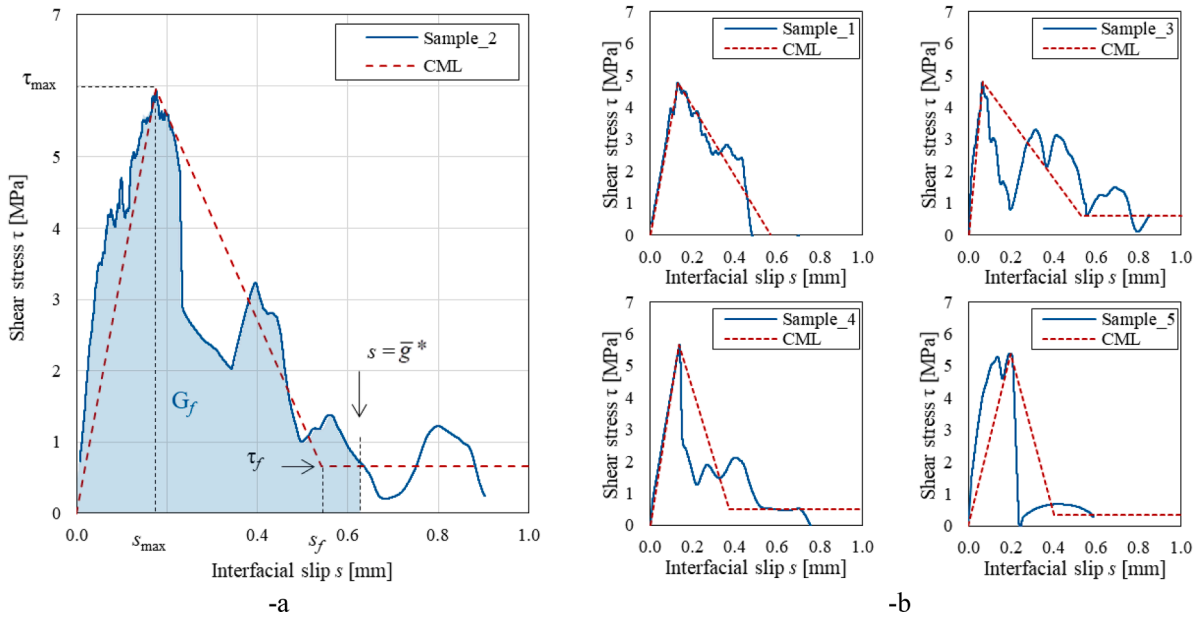


**Fig. 14.** Shear stress, τ - interface sliding, *s*, curves of SRG specimens: a) Sample_2; b) Sample_1, 3, 4 and 5.

measurement of the axial strain of fiber bundles, using strain gauges lined up along the specimen bonded length. From the obtained axial strain profiles, $\varepsilon(x)$, under the hypothesis of a pure Mode-II loading condition, the parametric relationship between bond stress $\tau(x)$ and corresponding slip $s$ $(x)$ can be obtained through suitable derivation and integration of the $\varepsilon(x)$ profile, respectively, according to the following equations:

$$\begin{cases} \tau(\bar{x}) = \dfrac{E_f A_{fs}}{p_{fs}} \dfrac{d\varepsilon(x)}{dx}\Big|_{x=\bar{x}} \\ s(\bar{x}) = \displaystyle\int_0^{\bar{x}} \varepsilon(x)dx \end{cases} \qquad 0 \le \bar{x} \le L \tag{44}$$

where $E_f$, $A_{fs}$ and $p_{fs}$ are the fiber bundle elastic modulus, area and perimeter, respectively (Fig. 9), whereas $L$ is the bonded length.

It is worth noting that a similar approach is adopted in the literature for adhesively-bonded FRP-substrate joints, where strain gauges are applied directly on the external face of the FRP reinforcement [18,42].

The use of stain gauges in DS tests of SRG specimens may be complicate due to the presence of the external matrix layer and to the reduced surface of steel strands; for this reason in [49] some indirect calibration methods of the $\tau(s)$ law from the load (or stress) response of direct shear tests were proposed, which proved to be effective in modeling the analytical interface bond-slip behavior. Similarly, in the present study, experimental $\tau(s)$ curves are determined by indirect calibration from the stress responses presented in Fig. 11-b, according to the analytical approach proposed by Zhu et al [6]. The adopted approach is based on the hypothesis of a rigid substrate and a pure Mode-II loading condition. Besides, the matrix-fiber interface is assumed to be subjected exclusively to shear stress, whereas peeling and bending effects are neglected.

As a result of the mentioned assumptions, by imposing the equilibrium of an infinitesimal portion of the matrix-fiber interface, the following Eq. (45) can be obtained:

$$\tau(s) = \frac{dP}{dg}\Big|_{g=s} \frac{P(s)}{E_f n^2 A_{fs} p_{fs}} \tag{45}$$

where $dP/dg$ indicates the first derivative of the applied load $P$ with respect to the global slip $g$, $E_f$, $A_{fs}$ and $p_{fs}$ are the fiber bundle elastic modulus, area and perimeter, respectively, whereas $n$ is the number of fiber bundles included in the textile layer.

**Table 3**
Tri-linear CML parameters of specimens Sample_1-5.

| Specimen name | $\tau_{max}$ [MPa] | $s_{max}$ [mm] | $\tau_f$ [MPa] | $s_f$ [mm] | $G_f$ [N/mm] |
|---|---|---|---|---|---|
| Sample_1 | 4.77 | 0.13 | – | 0.57 | 1.349 |
| Sample_2 | 5.95 | 0.18 | 0.66 | 0.55 | 1.731 |
| Sample_3 | 4.81 | 0.06 | 0.59 | 0.53 | 1.412 |
| Sample_4 | 5.66 | 0.14 | 0.49 | 0.37 | 1.117 |
| Sample_5 | 5.38 | 0.20 | 0.35 | 0.41 | 1.118 |
| Average: TRI-LINEAR CML | 5.31 | 0.14 | 0.52 | 0.49 | 1.35 |
| CoV [%] | 9.75 | 35.89 | 25.44 | 18.20 | 18.84 |

The experimental $\tau(s)$ curves of specimens Sample_1-5 obtained through Eq. (45) are presented synoptically in Fig. 14 (subfigure a depicts the typical behavior obtained).

As it can be deduced, Sample_1 was the only specimen exhibiting a null residual shear friction stress. This is attributed to the shape of the experimental *P-g* curve of Sample_1, which entailed for a marked load drop combined with a negative $dP/dg$ right after the onset of debonding.

As inferred by Fig. 14-a, the $\tau(s)$ curve is characterized by an initial ascending branch that roughly reflects an interface elastic behavior. After the attainment of the peak shear stress, the interface enters in the softening branch and the tangential stress $\tau(s)$ locally decreases increasing the slip. Eventually a sub horizontal branch can be identified in the $\tau(s)$ response, which is attributed to the friction exchanged at the matrix fiber interface after the onset of the cohesive interfacial crack.

The bond-slip behavior exhibited by Specimen_1-5 was similar to that experimentally observed by Carozzi et al. [51] in single-lap direct shear tests of PBO FRCM-masonry joints exhibiting cohesive debonding at the matrix-fiber interface. The $\tau(s)$ law of those specimens was approximated with a simplified tri-linear CML based on five parameters, namely the interface fracture energy $G_f$, the maximum shear stress $\tau_{max}$ and the corresponding interfacial sliding $s_{max}$, the frictional shear stress $\tau_f$ and the corresponding interfacial sliding $s_f$.

Table 3 reports the tri-linear CML parameters estimated from the experimental $\tau(s)$ curves of Fig. 14-a, according to the criterion shown in the same figure; $G_f$ is computed as the area below the curve until $s=\overline{g^*}$ ($\overline{g^*}$ = 0.63 mm, see Table 2), $\tau_{max}$ and $s_{max}$ are respectively the shear stress and interface slip associated to experimental $\tau(s)$ curve peak, $\tau_f$ is the average shear stress recorded in the portion $s \ge \overline{g^*}$, whereas the

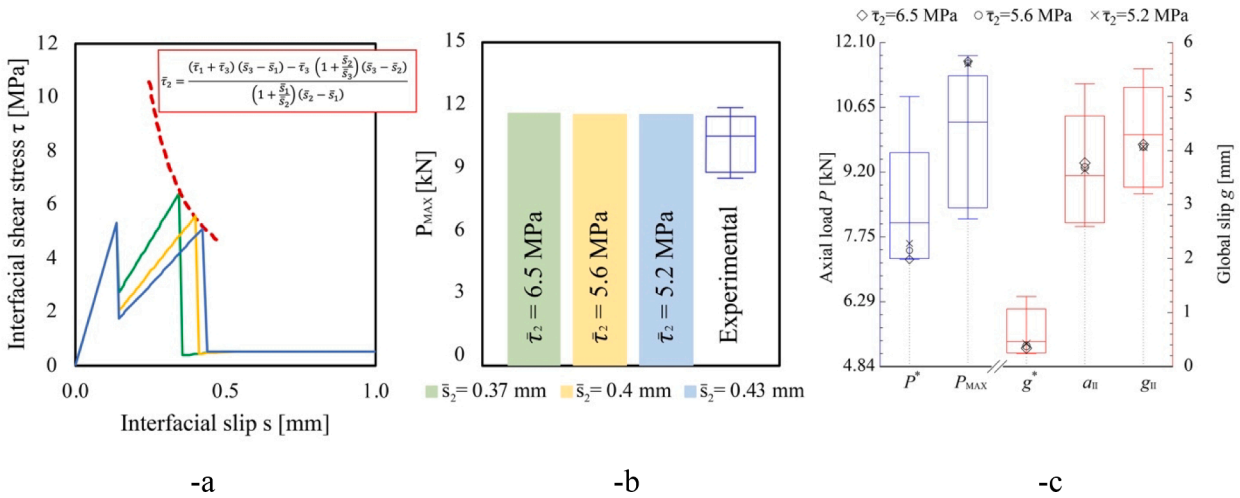


**Fig. 15.** -a: sawtooth models with equivalent fracture energy. The red curve shows in which point $\bar{\tau}_2$ must be placed, considering the condition $\bar{s}_1 < \bar{s}_2 < \bar{s}_3$, in order to maintain the same fracture energy of the trilinear model. -b: values of $\bar{\tau}_2$ and $\bar{s}_2$ adopted in the sensitivity analysis (greater the slip is, lower the shear stress and the stiffness are) compared with experimental results. -c: Box-plot of the representative *P-g* response experimental parameters compared with numerical predictions; on each box, the inner segment indicates the median, the bottom and top edges of the box indicate the 25th and 75th percentiles, respectively, whereas markers ◇, ○ and × represent the analytical model predictions for the *P-g* response parameters. (For interpretation of the references to colour in this figure legend, the reader is referred to the web version of this article.)

parameter $s_f$ is obtained as a function of the other four. The CML parameters reported in Table 3 are adopted in the sequel to model the trilinear CML curve showed in Fig. 14.

Noteworthy, for Samples 2 and 5 the described criterion provided an underestimation of the interface elastic behavior. This can be attributed to a nonlinearity observed in the experimental $\tau(s)$ curve before the attainment of the peak shear stress, as a result of load oscillations recorded in the ascending stage of corresponding *P-g* curves (see Fig. 11). The proposed calibration criterion provides for a linearization of the $\tau(s)$ curve elastic behavior, which is based on the three mutually dependent parameters $\tau_{max}$, $s_{max}$ and $k_1 = \tau_{max}/s_{max}$ (i.e. the slope of the CML elastic stage). Alternative calibration strategies can be adopted, e.g enforcing the parameter $k_1$, to reproduce specific features of the SRG-substrate joint. In addition, it should be pointed out that the experimental information available on the slip and shear stress is exclusively available at the loaded edge (indirect from experimental data) and therefore the calibration method used cannot be considered fully reliable in principle, but it is the only one that can be followed using a traditional set up of measurement.

## 4. Sawtooth model interface law: Tuning of the parameters and results

As pointed out in Section 2, the parameters to tune in the sawtooth model are 2, namely the tangential strength $\bar{\tau}_2$ of the interface in Phase 2 and the corresponding ultimate slip $\bar{s}_2$. The model is aimed at reproducing the response obtained assuming for the interface a trilinear continuous stress-slip relationship equipped with softening and residual strength. Even though any kind of interface law can be simulated, the comparison is done in such specific case because an analytical solution is already at disposal from the literature. Therefore, let us assume as reference a trilinear interface law, taking then the data reported in Table 1 and Table 3.

The two models -trilinear and sawtooth-, looking in particular at the response of the sawtooth model during the loading process as far as the distribution of tangential stresses at the interface is concerned (see also

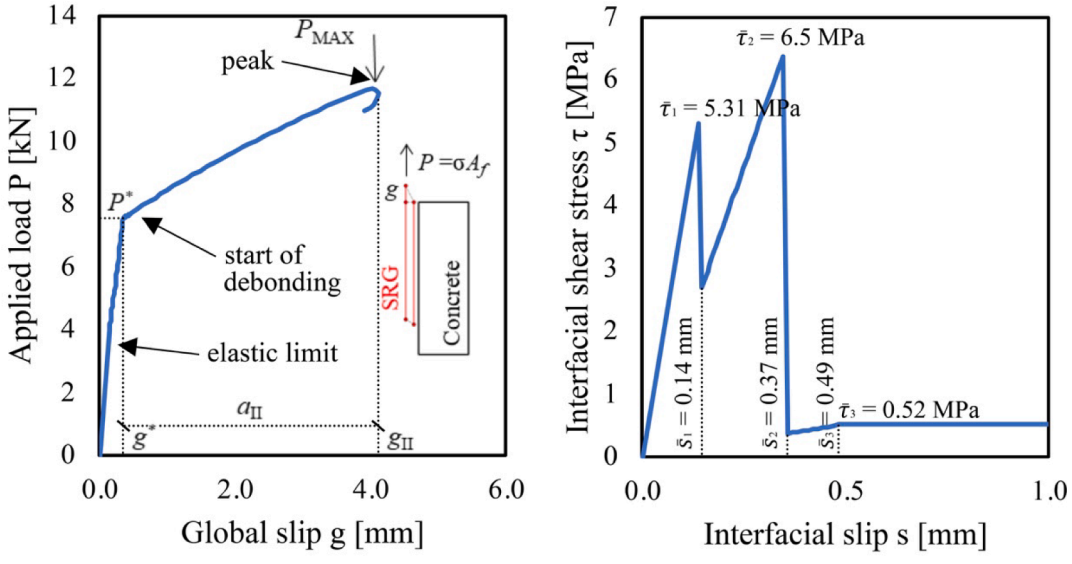


**Fig. 16.** typical global force–displacement curve (left) obtained with the sawtooth model (right).

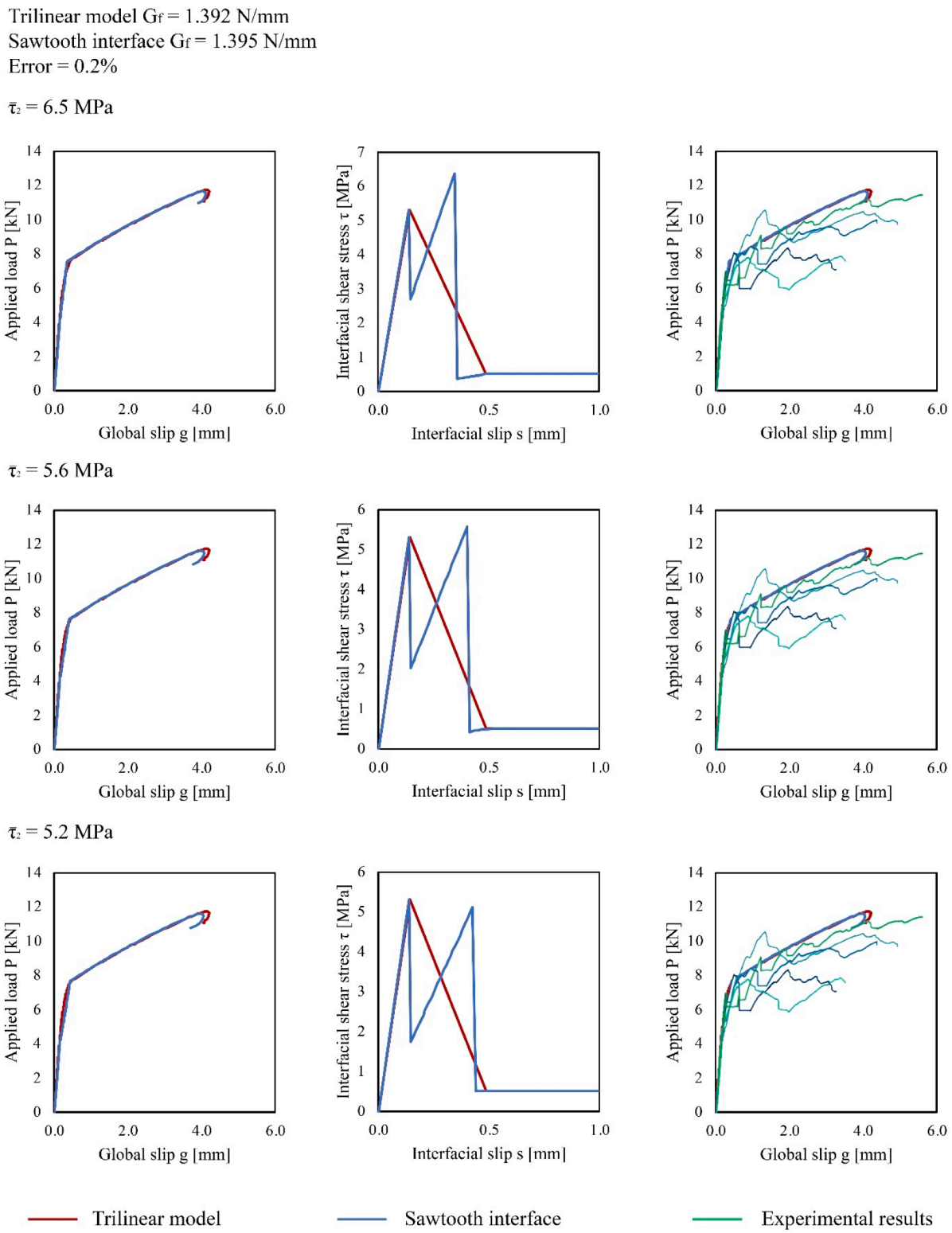


**Fig. 17.** Comparison among analytical sawtooth model, trilinear model and experimental data at 3 different values of..$\bar{\tau}_2$

Fig. 5 and Fig. 6), are equivalent if and only if the two fracture energies are identical.

Considering a trilinear relationship, its fracture energy $G_f^{TL}$ (excluding the residual strength) is equal to the following expression:

$$G_f^{TL} = \frac{\bar{\tau}_1 + \bar{\tau}_3}{2}(\bar{s}_3 - \bar{s}_1) \tag{46}$$

Conversely, the fracture energy of the sawtooth model $G_f^{ST}$ is the following:

$$G_f^{ST} = \frac{\bar{\tau}_2}{2}\left(1 + \frac{\bar{s}_1}{\bar{s}_2}\right)(\bar{s}_2 - \bar{s}_1) + \frac{\bar{\tau}_3}{2}\left(1 + \frac{\bar{s}_2}{\bar{s}_3}\right)(\bar{s}_3 - \bar{s}_2) \tag{47}$$

By equating the two fracture energies it is possible to find $\bar{\tau}_2$ at a selected slip $\bar{s}_2$ ranging between $\bar{s}_1$ and $\bar{s}_3$:

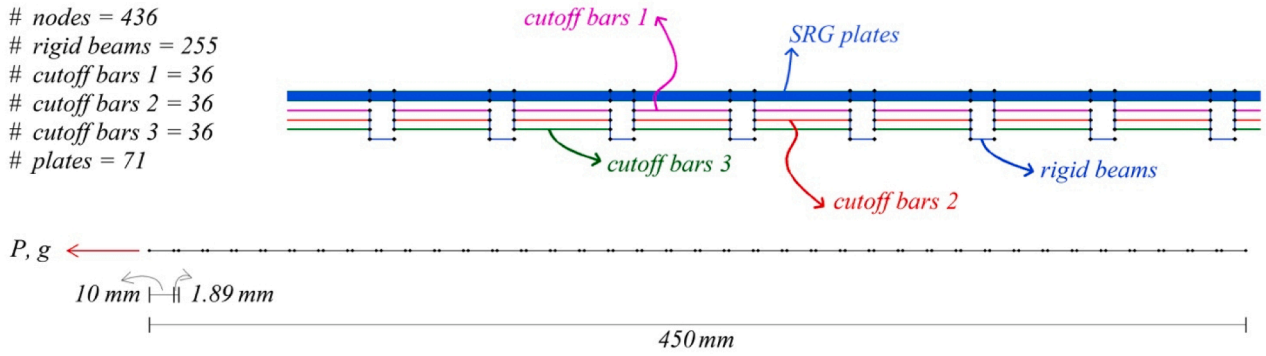


**Fig. 18.** FE model discretization used in the numerical implementation in a commercial software.

$$\bar{\tau}_2 = \frac{(\bar{\tau}_1 + \bar{\tau}_3)(\bar{s}_3 - \bar{s}_1) - \bar{\tau}_3\left(1 + \frac{\bar{\tau}_2}{\bar{\tau}_3}\right)(\bar{s}_3 - \bar{s}_2)}{\left(1 + \frac{\bar{\tau}_1}{\bar{s}_2}\right)(\bar{s}_2 - \bar{s}_1)} \tag{48}$$

In the specific case at hand, Eq. (48) is represented in Fig. 15-a with a dashed thick red line, along with three sawtooth interface laws having the same fracture energy and characterized by $\bar{\tau}_2$ respectively equal to 6.5, 5.6 and 5.2 MPa. The corresponding ultimate slips $\bar{s}_2$ are equal to 0.37, 0.40 and 0.43 mm respectively. As it is possible to notice from Fig. 15-a, the higher $\bar{s}_2$ is, the lower $\bar{\tau}_2$ turns out, and the lower the stiffness is. It is worth mentioning that the suggestiveness to expect that $\bar{\tau}_2$ is lower than $\bar{\tau}_1$ and equal (or similar) to that one of the trilinear model at the same slip $\bar{s}_2$ is not correct; in fact, the two models will perform globally in the same way if they dissipate the same fracture energy.

Looking at Fig. 15-c, where the numerical parameters representative of the *P*-*g* response are depicted and compared with experimental outcomes, it can stated that they remain essentially unchanged for the three different cases investigated. In particular, there is no variation of the peak load attained, Fig. 15-b, which confirms that trilinear models with the same fracture energy are associated to a pretty similar global response. As expected, more visible (but still very moderate) variations are observed for $P^*$, because such quantity is macroscopically related to the debonding activation, i.e. when Phase 2 is already active. Overall, the agreement with experimental data appears quite satisfactory.

Fig. 16 shows the results (global force–displacement curve of the reinforcement, sub-graph on the left) obtained assuming the sawtooth $\tau(x)$ - $s(x)$ interface law reported on the right, inspecting the behavior at many values of $l$ between 0 and $L$ (according to the procedure summarized in the flowchart of Fig. 4). It is worth noting that the observed trend of the force–displacement response at the loaded edge is typical for the model proposed and does not depend on the particular numerical data assumed to set the interface constitutive behavior. In addition, it is interesting to point out that the main features of the global debonding curve of Fig. 16 can be easily identified, determining meaningful load and slip quantities, such as $P^*$, $P_{MAX}$, $g_{II}$ and $g^*$. It is particularly clear the instant of triggering of the debonding until the attainment of the peak applied load; after the peak, softening and a rapid snap-back take place, again typical in such kind of models and already observed by many authors in the recent past. The last point of the curve, located immediately after the peak load but with a clear softening and a snap back already well developed, corresponds to the attainment at the free edge of the tangential stress $\tau(-L) = \bar{\tau}_1$. It is possible to continue the analyses following up the entire snap-back branch simply excluding Phase 1 and considering as independent variable $l_2$. When $l_2 = L$ then $\bar{\tau}_2$ is attained at the free edge, Phase 2 is no more active and independent variablebecomes $l_3$. Finally, when $l_3 = L$ the interface is all in phase 4 and the specimen indefinitely slips at constant applied load.

To corroborate such conclusion, in Fig. 17 a comparison in terms of global force–displacement, between analytical outcomes obtained by means of the sawtooth and the trilinear model is represented for the three cases aforementioned discussed. In the same figure the experimental results are also reported. As it is possible to notice, the agreement between the two models is perfect in every step of the analysis, starting from the linear range, proceeding with the activation of both softening and the debonding, and ending with the full separation of the interface. The agreement with experimental data appears satisfactory almost everywhere; particularly noticeable is the reliable reproduction of the inelastic pseudo-linear hardening phase, meaning that the adopted residual strength is quantitatively correct.

## 5. FE implementation in a commercial software

The FE implementation in a commercial software is discussed in this Section. Once that parameters $A_{fi}$, $E_{fi}$ and $F_{fi}$ are set, the two models (FE and sawtooth models) are identical; the only source of inaccuracy in the FE approach is the refinement of the mesh, which depends on the finite length $L_b$ assumed for the cutoff bars. The shortest $L_b$ is, the smallest the differences are.

The FE mesh adopted in the commercial FE model implementation is shown in Fig. 18. It is worth mentioning that the loaded edge is located on the left, whereas the free edge on the right, i.e. the loading conditions in the FE model are mirrored with respect to the analytical model. A not particularly refined discretization is used, assuming $L_b = 10$ mm, to show that reliable results can be obtained even without using models characterized by excessive computational burden.

The global FE response is compared with that of the sawtooth model in Fig. 19. The central column of subgraphs in Fig. 19 shows also a comparison for the interface constitutive laws adopted, in terms of equivalent force-slip constitutive curves of the CoBs, among FE (system of in-parallel trusses), sawtooth and trilinear models. It is particularly noticeable the perfect superposition of the laws used in the FE and sawtooth models. Looking at the global responses, the very good agreement among all models is worth mentioning. Indeed, the FE load–displacement curves approximate quite accurately the analytical models. The zigzagging behavior observed in the global response for the FE model is a typical consequence of the discretization, and tends to vanish refining further the mesh. The slight underestimation of both load carrying capacity and ultimate ductility is again linked to the level of mesh refinement. However, in general it can be stated that the procedure is rather reliable and, thanks to its theoretical simplicity, that it may be adopted in practical design.

The distribution of axial forces in the three CoBs at three relevant instants of the loading process in the FE model are depicted in Fig. 20, Fig. 21 and Fig. 22 for $\bar{\tau}_2$ respectively equal to 6.5, 5.6 and 5.2 MPa.

It is particularly evident the propagation of the debonding from point A (Phase 4 just started), to point C (full debonding), passing through point B, where about one half (left part) of the bond length is debonded from the substrate, as clearly visible from the value of the axial load in the third CoB, which is constantly equal to $F_{f3} = \bar{\tau}_3 p_f L_b$ (see Eq. (42)).

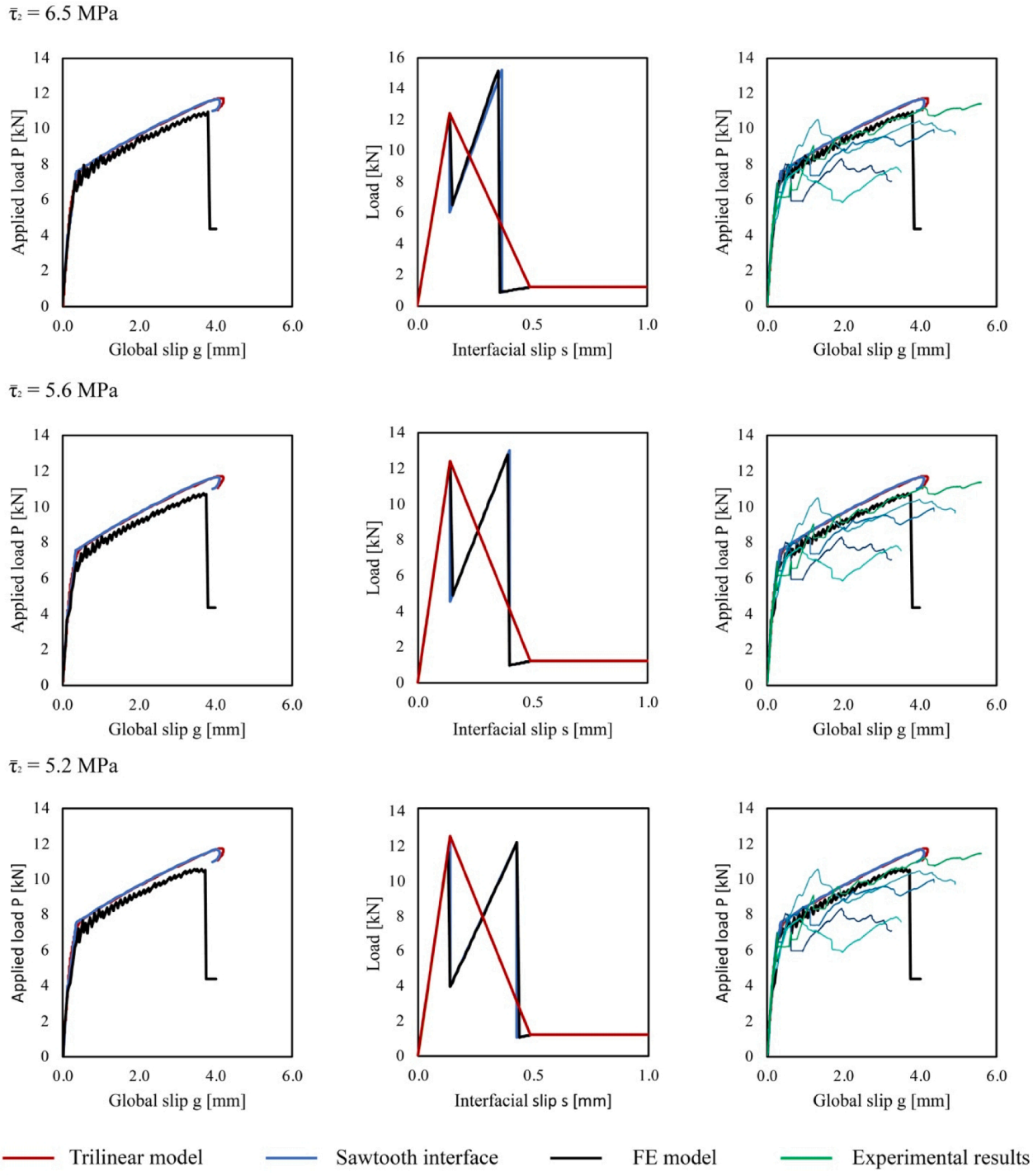


**Fig. 19.** FE model results for 3 different $\bar{\tau}_2$ values: comparison among trilinear model, sawtooth model and experimental results.

For the sake of completeness, in Fig. 23, the slip shape along the bond length is represented for points A, B and C (only the case where $\bar{\tau}_2$ is assumed equal to 6.5 MPa is reported). Such slip, in the FE model, is simply equal to the displacement of the nodes belonging to the elastic steel elements. As can be noted, all elements located in the debonded region exhibit displacements that grow parabolically starting from the point of activation of the last Phase 4, see Eq. (35).

## 6. Conclusions

A closed form sawtooth interface model for SRG-reinforced infinitely stiff and resistant supports subjected to direct shear tests has been presented, with a straightforward implementation into a commercial FE code that does not need any plug-in subroutine.

The tangential stress-slip interface relationship is multi-linear and discontinuous, constituted by three initial elastic phases with progressively degraded stiffness and a final perfectly plastic phase modelling the residual strength at the interface. The FE implementation proposed is constituted by the assemblage of two elasto-fragile trusses disposed in parallel and one elasto-ductile, transversally linked by rigid beams connected also to the support and the steel grid, assumed linear elastic.

The model, both in its sawtooth and FE version has been validated

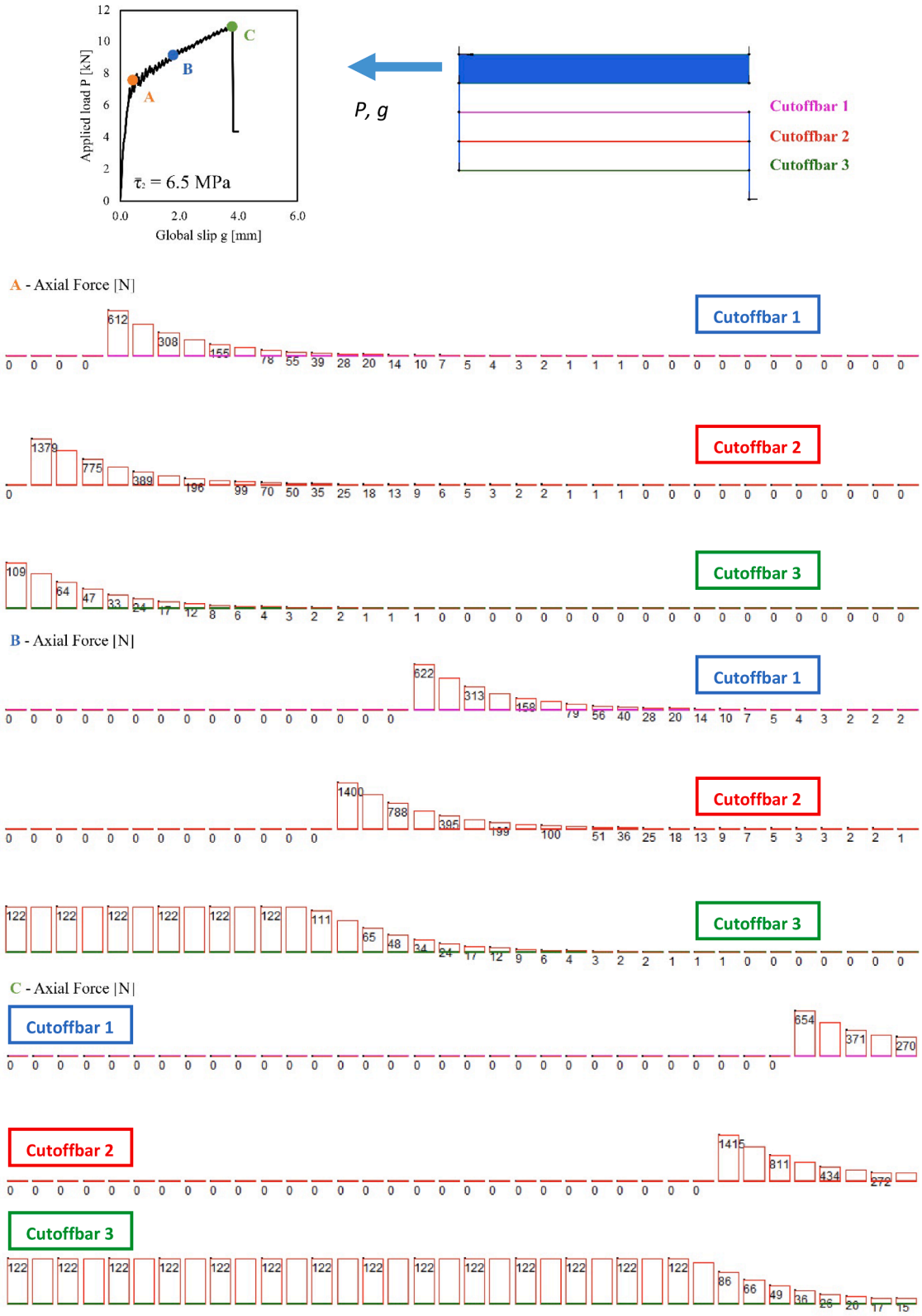


**Fig. 20.** FE model with $\bar{\tau}_2 = 6.5$ MPa, axial forces on CoBs at three relevant instants of the loading process.

against an already existent trilinear model of interface and experimental data, specifically carried out by the authors for comparison purposes. Experimentation -carried out by the authors exclusively for validation purposes of the analytical/numerical approach discussed- has relied into testing 5 samples of SRG-reinforced concrete specimens subjected to single lap shear tests.

The main advantages in proposing the present sawtooth and FE models stand into (i) the possibility to use a standard and low cost FE software -without the need of additional subroutines- to carry out speedy numerical analyses to predict the debonding behavior of SRG-reinforced specimens, (ii) the increased robustness of the algorithm when compared with more sophisticated approaches and its high

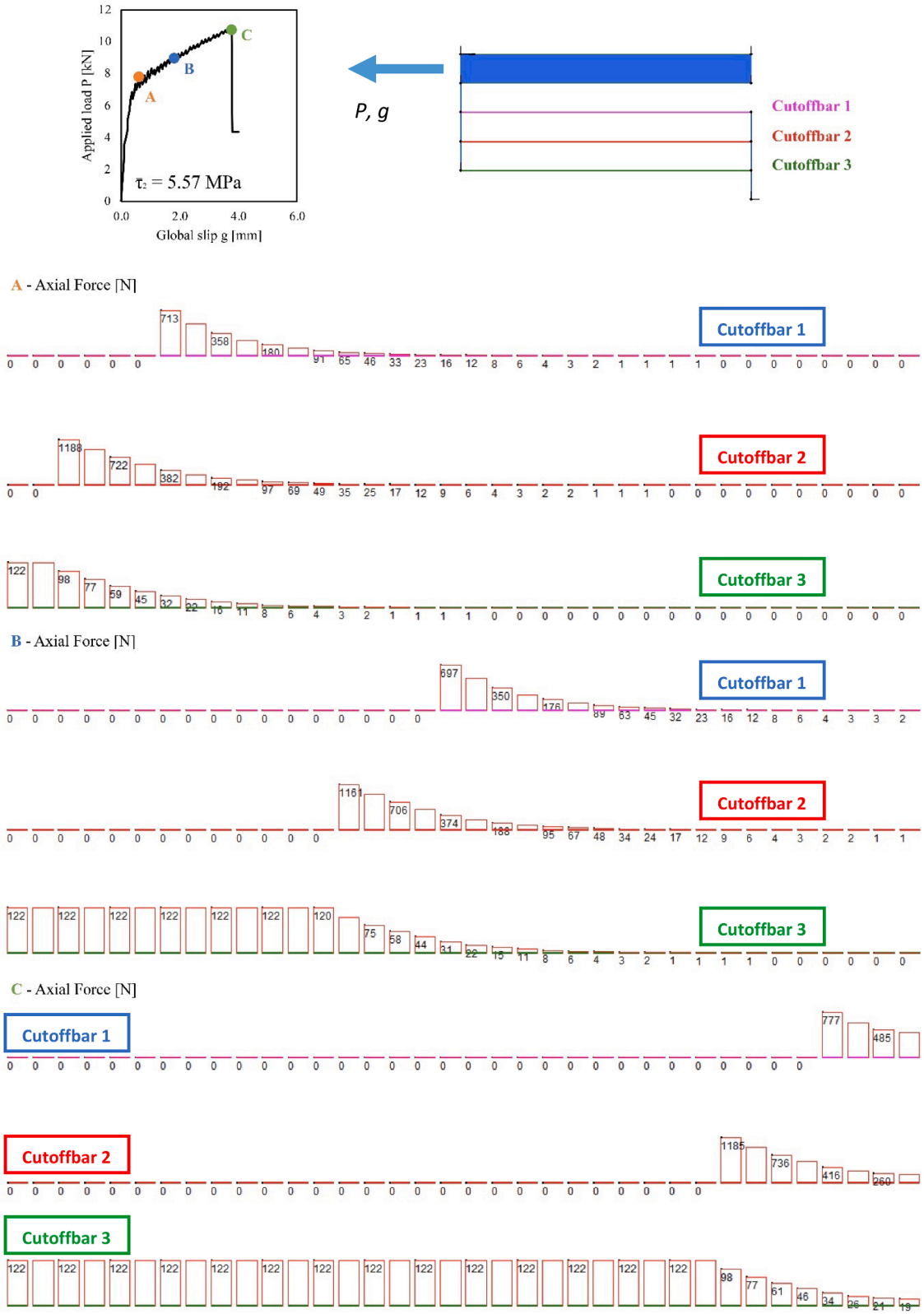


**Fig. 21.** FE model with $\bar{\tau}_2 = 5.6$ MPa, axial forces on CoBs at three relevant instants of the loading process.

reliability, (iii) the possibility of utilization in common design even by users not familiar with complex numerical issues associated with the intrinsic difficulties to deal with softening materials and interfaces, (iv) the possibility of analyzing entire reinforced structures and structural elements without the need of implementing ad-hoc subroutines to take into account the presence of interface FEs representing the interaction between grid and support characterized by a non-linear constitutive behavior which is non-standard.

When compared with existing sawtooth models recently proposed in the literature for the analysis of the debonding of FRP, the implementation of more phases and a final residual strength should be considered a major advancement of the research. As far as the global

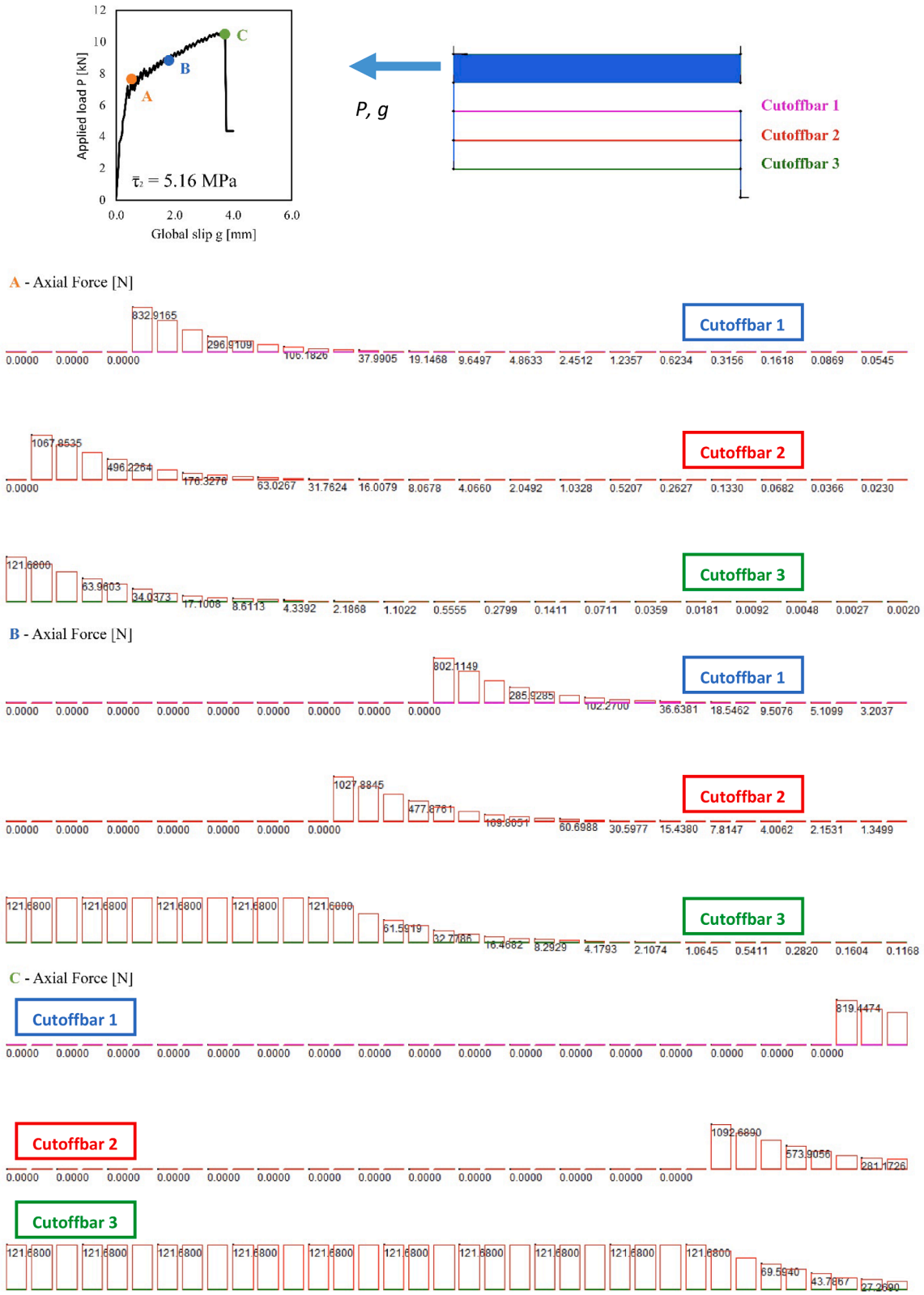


**Fig. 22.** FE model with $\bar{\tau}_2 = 5.2$ MPa, axial forces on CoBs at three relevant instants of the loading process.

behavior is concerned, indeed, the response of a specimen reinforced with TRM is more complex than that of the same one reinforced with FRP, mainly because when TRM is present, a hardening is usually observed during the debonding process, which physically is associated to the activation of the residual tangential strength of the interface. Such feature cannot be correctly reproduced with the utilization of two or more than two elastic phases representing the interface behavior.

Future developments include -but are not limited to- the following extensions of the present model:

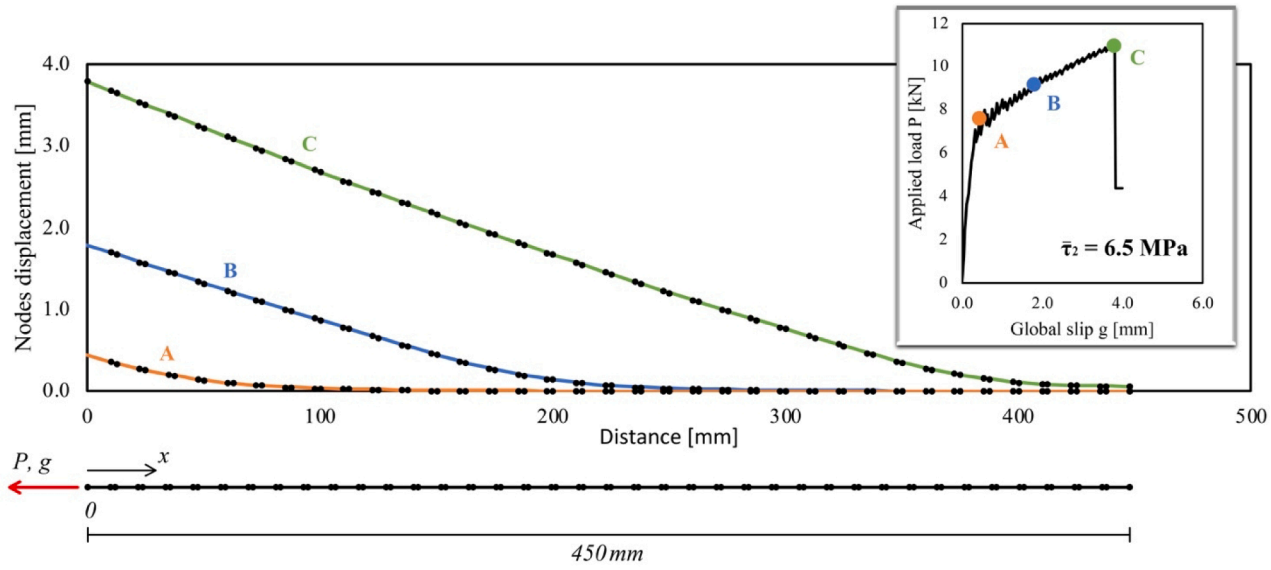


**Fig. 23.** FE model with $\bar{\tau}_2 = 6.5$ MPa, slip of the elastic steel layer at three relevant instants of the loading process (A: initial debonding; B: intermediate debonding; C: almost full debonding).

- study of the debonding behavior of curved specimens reinforced with FRCM, an issue particularly important when dealing with the strengthening of masonry arches.
- The introduction of elasto-brittle elements to simulate the presence of the external and internal layers of mortar.
- The FE analysis of real structural elements and structures, e.g. shear walls, entire vaults and out-of-plane loaded panels in two-way bending, simulating the reinforcement directly into a FE commercial software by means of the model constituted by in-parallel cutoff bars, elastic trusses and rigid connection beams. In this regard, the clear advantage is to offer to the user a procedure characterized by high numerical stability in problems exhibiting strong local softening.
- The introduction of anchoring systems, a topic which represents an ongoing research strength which is being tackled by means of a combined experimental and theoretical approach.

Data availability statement.

The authors declare that the reproducibility of the model is secured by implementing the algorithm reported in Section 3 (with particular regard to Eqs. (1)-(48)). Results of the experimental data used to validate the model proposed are available in Fig. 11.

## CRediT authorship contribution statement

**Natalia Pingaro:** Methodology, Software, Validation, Formal analysis, Investigation, Data curation, Writing – original draft, Writing – review & editing, Visualization. **Angelo Savio Calabrese:** Methodology, Validation, Formal analysis, Investigation, Resources, Data curation, Writing – original draft, Writing – review & editing, Visualization. **Gabriele Milani:** Conceptualization, Methodology, Software, Validation, Formal analysis, Investigation, Writing – original draft, Writing – review & editing, Supervision. **Carlo Poggi:** Methodology, Formal analysis, Investigation, Data curation, Writing – original draft, Writing – review & editing, Supervision, Project administration, Funding acquisition.

## Declaration of Competing Interest

The authors declare that they have no known competing financial interests or personal relationships that could have appeared to influence the work reported in this paper.

## Data availability

Data will be made available on request.

## References

[1] Papanicolaou CG, Triantafillou TC, Karlos K, Papathanasiou M. Textile-reinforced mortar (TRM) versus FRP as strengthening material of URM walls: in-plane cyclic loading. Mater Struct 2007;40:1081–97. https://doi.org/10.1617/s11527-006-9207-8.
[2] Ghiassi B. Mechanics and durability of lime-based textile reinforced mortars. RILEM Tech Lett 2019;4:130–7. https://doi.org/10.21809/rilemtechlett.2019.99.
[3] Dalalbashi A, Ghiassi B, Oliveira DV. Textile-to-mortar bond behaviour in lime-based textile reinforced mortars. Constr Build Mater 2019:227. https://doi.org/10.1016/j.conbuildmat.2019.116682.
[4] De Santis S, Ceroni F, de Felice G, Fagone M, Ghiassi B, Kwiecień A, et al. Round Robin Test on tensile and bond behaviour of Steel Reinforced Grout systems. Compos B Eng 2017;127:100–20. https://doi.org/10.1016/j.compositesb.2017.03.052.
[5] Grande E, Imbimbo M, Sacco E. Numerical investigation on the bond behavior of FRCM strengthening systems. Compos B Eng 2018;145:240–51. https://doi.org/10.1016/j.compositesb.2018.03.010.
[6] Zhu M, Ueda T, Zhu J-H. Generalized Evaluation of Bond Behavior of the Externally Bonded FRP Reinforcement to Concrete. J Compos Constr 2020;24:04020066. https://doi.org/10.1061/(ASCE)CC.1943-5614.0001081.
[7] Colombi P, Bocciarelli M, Calabrese AS, D'Antino T, Papa T. Externally bonded CFRP reinforcement of steel structures: mechanical characterization of a toughened epoxy adhesive, Shanghai: 2022.
[8] Ghiassi B, Xavier J, Oliveira DV, Lourenço PB. Application of digital image correlation in investigating the bond between FRP and masonry. Compos Struct 2013;106:340–9. https://doi.org/10.1016/j.compstruct.2013.06.024.
[9] Bertolesi E, Fagone M, Rotunno T, Grande E, Milani G. Experimental characterization of the textile-to-mortar bond through distributed optical sensors. Constr Build Mater 2022;326:126640. https://doi.org/10.1016/j.conbuildmat.2022.126640.
[10] Calabrese AS, Colombi P, D'Antino T. Analytical solution of the bond behavior of FRCM composites using a rigid-softening cohesive material law. Compos B Eng 2019;174:1–10. https://doi.org/10.1016/j.compositesb.2019.107051.
[11] Calabrese AS, D'Antino T, Colombi P. Experimental and analytical investigation of PBO FRCM-concrete bond behavior using direct and indirect shear test set-ups. Compos Struct 2021:267. https://doi.org/10.1016/j.compstruct.2021.113672.
[12] Carloni C, D'Antino T, Sneed LH, Pellegrino C. Role of the Matrix Layers in the Stress-Transfer Mechanism of FRCM Composites Bonded to a Concrete Substrate. J Eng Mech 2015;141:04014165. https://doi.org/10.1061/(ASCE)EM.1943-7889.0000883.
[13] D'Antino T, Colombi P, Carloni C, Sneed LH. Estimation of a matrix-fiber interface cohesive material law in FRCM-concrete joints. Compos Struct 2018;193:103–12. https://doi.org/10.1016/j.compstruct.2018.03.005.

[14] Yuan Y, Milani G. Closed-form model for curved brittle substrates reinforced with FRP strips. Compos Struct 2023;304:116443. https://doi.org/10.1016/j.compstruct.2022.116443.
[15] Martinelli E. Closed-Form Solution Procedure for Simulating Debonding in FRP Strips Glued to a Generic Substrate Material. Fibers 2021;9:22. https://doi.org/10.3390/fib9040022.
[16] Bertolli V, D'Antino T. Modeling the behavior of externally bonded reinforcement using a rigid-trilinear cohesive material law. Int J Solids Struct 2022;248:111641. https://doi.org/10.1016/j.ijsolstr.2022.111641.
[17] Capozucca R, Ernesto G, Milani G, Bertolesi E. Fully analytical model for the analysis of externally bonded composites applied to brittle supports: sensitivity analysis. Int J Masonry Res Innov 2022;1:1. https://doi.org/10.1504/IJMRI.2022.10046112.
[18] Milani G, Fagone M, Rotunno T, Grande E, Bertolesi E. Development of an interface numerical model for C-FRPs applied on flat and curved masonry pillars. Compos Struct 2020;241:112074. https://doi.org/10.1016/j.compstruct.2020.112074.
[19] Bertolesi E, Grande E, Fagone M, Milani G, Rotunno T. Mechanical model based on a BVP for FRPs applied on flat and curved masonry pillars with anchor spikes. Compos Struct 2021;273:114251. https://doi.org/10.1016/j.compstruct.2021.114251.
[20] Biscaia HC, Chastre C, Silva MAG. Bond-slip model for FRP-to-concrete bonded joints under external compression. Compos B Eng 2015;80:246–59. https://doi.org/10.1016/j.compositesb.2015.06.004.
[21] Biscaia HC, Chastre C, Silva MAG. Nonlinear numerical analysis of the debonding failure process of FRP-to-concrete interfaces. Compos B Eng 2013;50:210–23. https://doi.org/10.1016/j.compositesb.2013.02.013.
[22] Carrara P, Ferretti D. A finite-difference model with mixed interface laws for shear tests of FRP plates bonded to concrete. Compos B Eng 2013;54:329–42. https://doi.org/10.1016/j.compositesb.2013.05.030.
[23] Milani G, Grande E. Simple bisection procedure in quickly convergent explicit ODE solver to numerically analyze FRCM strengthening systems. Compos B Eng 2020;199:108322. https://doi.org/10.1016/j.compositesb.2020.108322.
[24] Scacco J, Milani G, Lourenço PB. A micro-modeling approach for the prediction of TRM bond performance on curved masonry substrates. Compos Struct 2021;256:113065. https://doi.org/10.1016/j.compstruct.2020.113065.
[25] Grande E, Milani G. Procedure for the numerical characterization of the local bond behavior of FRCM. Compos Struct 2021;258:113404. https://doi.org/10.1016/j.compstruct.2020.113404.
[26] Zhang D, Yang J, Chi LY. The Bond-Slip Relationship at FRP-to-Brick Interfaces under Dynamic Loading. Materials (Basel) 2021;14:545. https://doi.org/10.3390/ma14030545.
[27] Ceroni F, de Felice G, Grande E, Malena M, Mazzotti C, Murgo F, et al. Analytical and numerical modeling of composite-to-brick bond. Mater Struct 2014;47:1987–2003. https://doi.org/10.1617/s11527-014-0382-8.
[28] Razavizadeh A, Ghiassi B, Oliveira DV. Bond behavior of SRG-strengthened masonry units: Testing and numerical modeling. Constr Build Mater 2014;64:387–97. https://doi.org/10.1016/j.conbuildmat.2014.04.070.
[29] Grande E, Milani G. Interface modeling approach for the study of the bond behavior of FRCM strengthening systems. Compos B Eng 2018;141:221–33. https://doi.org/10.1016/j.compositesb.2017.12.052.
[30] Grande E, Ghiassi B, Imbimbo M. Chapter 19 - Theoretical and FE models for the study of the bond behavior of FRCM systems. In: Ghiassi B, Milani G, editors. Numerical Modeling of Masonry and Historical Structures, Woodhead Publishing; 2019, p. 685–712. https://doi.org/10.1016/B978-0-08-102439-3.00019-1.
[31] Ghiassi B, Oliveira DV, Lourenço PB, Marcari G. Numerical study of the role of mortar joints in the bond behavior of FRP-strengthened masonry. Compos B Eng 2013;46:21–30. https://doi.org/10.1016/j.compositesb.2012.10.017.
[32] Grande E, Imbimbo M. A simple 1D-Finite Element approach for the study of the bond behavior of masonry elements strengthened by FRP. Compos B Eng 2016;91:548–58. https://doi.org/10.1016/j.compositesb.2016.02.005.
[33] Milani G. Simple model with in-parallel elasto-fragile trusses to characterize debonding on FRP-reinforced flat substrates. Compos Struct 2022;296:115874. https://doi.org/10.1016/j.compstruct.2022.115874.
[34] Pari M, Van de Graaf AV, Hendriks MAN, Rots JG. A multi-surface interface model for sequentially linear methods to analyse masonry structures. Eng Struct 2021;238:112123. https://doi.org/10.1016/j.engstruct.2021.112123.
[35] Yu C, Hoogenboom P, Rots J. Extension of incremental sequentially linear analysis to geometrical non-linearity with indirect displacement control. Eng Struct 2021;229:111562. https://doi.org/10.1016/j.engstruct.2020.111562.
[36] Pari M, Swart W, van Gijzen Mb, Hendriks Man, Rots Jg. Two solution strategies to improve the computational performance of sequentially linear analysis for quasi-brittle structures. Int J Numer Meth Eng 2020;121:2128–46. https://doi.org/10.1002/nme.6302.
[37] Pari M, Hendriks MAN, Rots JG. Non-proportional loading in sequentially linear solution procedures for quasi-brittle fracture: A comparison and perspective on the mechanism of stress redistribution. Eng Fract Mech 2020;230:106960. https://doi.org/10.1016/j.engfracmech.2020.106960.
[38] Yu C, Hoogenboom PCJ, Rots JG. Incremental sequentially linear analysis to control failure for quasi-brittle materials and structures including non-proportional loading. Eng Fract Mech 2018;202:332–49. https://doi.org/10.1016/j.engfracmech.2018.07.036.
[39] Zou X, Sneed L, D'Antino T. Full-range behavior of fiber reinforced cementitious matrix (FRCM)- concrete joints using a trilinear bond-slip relationship. Compos Struct 2020;239:112024. https://doi.org/10.1016/j.compstruct.2020.112024.
[40] Wu Z, Yuan H, Niu H. Stress Transfer and Fracture Propagation in Different Kinds of Adhesive Joints. J Eng Mech 2002;128:562–73. https://doi.org/10.1061/(ASCE)0733-9399(2002)128:5(562).
[41] Yuan H, Teng JG, Seracino R, Wu ZS, Yao J. Full-range behavior of FRP-to-concrete bonded joints. Eng Struct 2004;26:553–65. https://doi.org/10.1016/j.engstruct.2003.11.006.
[42] Yu T, Fernando D, Teng JG, Zhao XL. Experimental study on CFRP-to-steel bonded interfaces. Compos B Eng 2012;43:2279–89. https://doi.org/10.1016/j.compositesb.2012.01.024.
[43] De Lorenzis L, Zavarise G. Interfacial stress analysis and prediction of debonding for a thin plate bonded to a curved substrate. Int J Non Linear Mech 2009;44:358–70. https://doi.org/10.1016/j.ijnonlinmec.2009.01.002.
[44] EOTA. EAD 340275-00-0104: Externally-bonded composite systems with inorganic matrix for strengthening of concrete and masonry structures 2018.
[45] Kerakoll. Technical datasheet of GeoSteel G600 2020.
[46] Kerakoll. Technical datasheet of GeoLite 2019.
[47] EN 12390-3:2019. Testing hardened concrete - Part 3: Compressive strength of test specimens. 2019.
[48] EN 12390-6:2009. Testing hardened concrete - Part 6: Tensile splitting strength of test specimens. 2009.
[49] Santandrea M, Focacci F, Mazzotti C, Ubertini F, Carloni C. Determination of the interfacial cohesive material law for SRG composites bonded to a masonry substrate. Eng Fail Anal 2020:111. https://doi.org/10.1016/j.engfailanal.2019.104322.
[50] Ombres L, Mancuso N, Mazzuca S, Verre S. Bond between Carbon Fabric-Reinforced Cementitious Matrix and Masonry Substrate. J Mater Civ Eng 2019;31:04018356. https://doi.org/10.1061/(ASCE)MT.1943-5533.0002561.
[51] Carozzi FG, Colombi P, Fava G, Poggi C. A cohesive interface crack model for the matrix–textile debonding in FRCM composites. Compos Struct 2016;143:230–41. https://doi.org/10.1016/j.compstruct.2016.02.019.